Drag reduction mechanism of a diving submersible with the double-row silk appendages based on Continuous Wavelet Transform and Dynamic Modal Decomposition

Fei YAN^a, Shan WANG^a, Zhiyin YANG^b, Akira RINOSHIKA ^{c,*}, Jian ZHANG^{a,*}

^aSchool of Mechanical Engineering, Jiangsu University of Science and Technology, Zhenjiang

212000, China

^bSchool of Engineering, University of Derby, Derby DE22 3AW, United Kingdom

^cHangzhou International Innovation Institute, Beihang University, 166 Shuanghongqiao

Street, Pingyao Town, Yuhang District, Hangzhou 311115, China

Corresponding author:

Prof. Akira RINOSHIKA, E-mail: liluhui@buaa.edu.cn

Prof. Jian ZHANG, E-mail:zhjian127@just.edu.cn

Abstract:

This study presents a method to reduce drag and enhance the diving velocity of a submersible through the application of a double-row of silk appendages on its surface. Initially, Computational fluid dynamics (CFD) simulations reveal that boundary layer separation occurs in the midship of a conventional submersible, accompanied by significant vortex formation at the bow and stern. Thus, a double-row of silk appendages is applied to suppress boundary layer separation and modify the vortex structures in the wake. Torque sensors and particle image velocimetry (PIV) systems are employed to measure the drag force and wake flow field. The results show that the silk appendages effectively suppress adverse pressure gradient-induced boundary layer separation. Moreover, the wake structure is optimized, leading to a drag reduction of up to 6.67%. To investigate the underlying mechanism, continuous wavelet transform (CWT) and dynamic mode decomposition (DMD) methods are applied. The analysis indicates that a double-row of silk appendages with appropriate length reduces low-frequency modal energy, suppresses flow separation and large-scale vortices, promotes small-scale vortex structures, and improves flow field stability. However, longer appendages may intensify local disturbances, resulting in decreased stability.

Keywords: Submersible; Silk appendage; Drag reduction; Particle image velocimetry; Dynamic mode decomposition; Continuous wavelet transform;

1. Introduction

The rapid development of deep-sea exploration and underwater engineering technologies has led to growing demands for enhanced performance in submersibles, which serve as critical equipment for marine scientific research, resource exploration, and military applications (Du et

al., 2021). The diving efficiency of submersibles is directly linked to their operational effectiveness and mission reliability. However, traditional submersibles face significant challenges, including a substantial rise in drag and flow field destabilization during high-speed dives, which severely limit their performance (Zhai et al., 2024). Therefore, developing effective fluid drag reduction methods is essential for improving the operational performance of submersibles (Chen et al., 2023; Li et al., 2024).

Existing drag reduction techniques are mainly divided into active and passive approaches. Active drag reduction involves regulating the flow field using methods such as plasma-synthesized jets (Xie et al., 2021), microbubble injection, or surface vibration (Luo et al., 2015). Although these approaches allow dynamic response, their practical application is often constrained by high energy consumption and system complexity. In contrast, passive drag reduction techniques are considered more promising for submersibles due to their no external energy requirement. Typical methods include vortex generators, microgroove surfaces (Monfared Mosghani et al., 2023), drag control via delayed laminar-turbulent transition (Durbin and Wu, 2007), and wake structures optimization (Cui et al., 2015). While these techniques are relatively easy to implement and cost-effective (Su et al., 2012), they often suffer from limited durability and adaptability to complex flow fields (Nouri et al., 2024). In comparison, silk appendages can adaptively adjust the pressure gradient and vortex evolution through their dynamic deformation (Ahmad et al., 2015), offering distinct advantages in handling complex working conditions.

In recent years, considerable advances have been achieved in understanding the drag reduction mechanisms of of flexible appendage. Tian et al. introduced a silk-based wake modulation method, which attained a drag reduction rate of approximately 10% by suppressing large-scale vortex shedding in the wake of a flat plate model (Gao et al., 2020; Tian, 2021). Mao et al. (2023) identified three oscillating modes and demonstrated that oscillating and undulating modes, particularly with filaments oscillating out of phase, are effective in reducing drag. Yan et al. (2025a, 2025b) mounted hair and silk appendages on the leading edge and midbody of a submersible, respectively. Their results revealed that these appendages mitigate flow disturbances in the wake, effectively breaking down large-scale vortices into smaller structures, thereby reducing turbulence intensity and enhancing wake characteristics. However, their work focused predominantly on qualitative wake observations, with limited quantitative assessment of drag reduction and little exploration of the underlying interaction mechanism between silk appendages and the turbulent boundary layer. Addressing these gaps, the present study extends prior research by providing a quantitative investigation into the physical mechanisms of silk-turbulence interactions, clearly establishing a causal relationship between modal-scale energy redistribution and the drag reduction effect.

On the other hand, drawing from boundary layer theory (Tao et al., 2024), Perry et al. (1966a, 1966b) proposed that the adverse pressure gradient profoundly modifies the turbulent boundary layer structure. Tanarro et al. (2019) further investigated the effect of adverse pressure gradient on the turbulent boundary layer over an airfoil surface, noting a reduction in the scale of organized turbulent structures. Building upon these foundational insights and to address the identified research gaps, a double-row silk appendage configuration is employed in this study to suppress boundary layer separation and disrupt wake vortex structures.

The selection of an appropriate material for the silk appendage is critical for the experimental

validity. Since the submersible functions in underwater environments, the appendage material must be hydrophobic and sufficiently flexible. Good hydrophobicity contributes to reducing adverse effects on submersible performance, while high elasticity and toughness ensure that the silk appendages maintain stable performance under complex flow conditions. According to literature, silk has a density between 1.1 to 1.4 g/cm^3 (Nguyen et al., 2019), a tensile strength ranging from 0.3 to 0.5 GPa, and a Young's modulus of 10- 17 GPa (Vepari and Kaplan, 2007; Wang et al., 2019; Zhang et al., 2021), offering favorable ductility alongside high strength. Furthermore, previous studies have indicated that silk appendages significantly disrupt the submersible wake flow (Yan et al., 2025a). Although synthetic alternatives exist, silk is widely regarded for its unique combination of flexibility and biocompatibility. Therefore, 320-denier silk was selected as the appendage material in this study.

With the rapid advancement of computational fluid dynamics (CFD), high-fidelity simulation of complex flows around submersibles has become feasible (Zhang et al., 2013; Boe et al., 2013), enabling the revelation of flow field characteristics that are challenging to capture experimentally. Given that the wake field of a submersible equipped with a silk appendage is expected to be more complex than that of a conventional submersible, advanced flow analysis techniques are required to investigate its characteristics. The dynamic mode decomposition (DMD) method enables decomposition of the velocity field and fluid motion into dynamic modes across multiple frequency scales (Chen et al., 2012), thereby revealing energy transfer processes within the flow. Li et al. (2023) demonstrated that DMD can effectively reconstruct the flow field of a pump-jet propeller, while Song et al. (2023) applied DMD to analyze the flow around a submersible under straight-line navigation, clarifying the vortex distribution in

the wake. The continuous wavelet transform (CWT) is particularly suitable for analyzing non-stationary fluid signals due to its time-frequency localization and multi-resolution capabilities (Farge et al., 1999). Zhao et al. (2012) used wavelet transforms to identify vortex-induced vibration frequencies, demonstrating the utility of wavelet analysis in fluid dynamics. Combining CWT and DMD significantly enhances the understanding of nonlinear, time-varying fluid behavior and complex flow dynamics.

To reduce drag during submersible descent, this study proposes a novel silk appendage installation approach. A double-row of silk appendages is arranged along the surface to suppress boundary layer separation and disrupt wake vortex structures, thereby achieving drag reduction. First, the flow field around the submersible is investigated through CFD simulations, which determine the installation scheme of the silk appendage. Subsequently, drag and wake measurements are conducted using a torque sensor and particle image velocimetry (PIV). Furthermore, DMD and CWT methods are employed to elucidate the underlying drag reduction mechanisms of the silk appendages.

2. Experimental setup

2.1 Submersible drag test system

This study focuses on the vertical diving condition of the submersible. The schematic diagram of the experimental setup and the physical model are shown in Fig. 1. The drag tests are performed in a recirculating water tank, comprising a pump, piping, and a test section fitted with a transparent acrylic panel for laser illumination and particle image velocimetry (PIV) measurements. The test section has a length of 2.5 m and a cross-sectional area of 0.6 $m \times 0.6$ m, providing an effective experimental volume of 0.3 m^2 . A multi-layer flow-straightening

screen is installed along the channel from upstream to downstream, which reduces the turbulence intensity to below 0.5%. The torque sensor used in the drag tests is a HYNJ-030 flange-type static torque sensor, with a range of 0-20 N·m and a measurement accuracy of $\pm 0.3\%$ F.S. The HY-XSA single-channel digital weighing transmitter is used for signal transmission, operating at a voltage of 10-30 V (DC) and a sampling frequency of 640 Hz.

To ensure a stable and fully developed flow field within the test section, minimize free-surface effects, and provide high-quality torque and PIV signals, a free-stream velocity of U=0.3~m/s was selected, corresponding to a Reynolds number of 65,749 ($Re=\rho UL/\mu$), where the water density ρ is 998.2 kg/m^3 , the characteristic length L is 220 mm, and the dynamic viscosity coefficient μ is $1.002\times10^{-3}Pa\cdot s$. This Reynolds number represents a balance between experimental feasibility and the capture of key flow phenomena relevant to actual submersible operations. Although real deep-sea conditions typically involve higher Reynolds numbers ($Re>10^6$), flow visualization experiments and numerical simulations indicate that the selected numerical values are sufficient to form a fully turbulent boundary layer, including characteristic phenomena such as boundary layer separation and periodic vortex shedding.

2.2 High speed PIV measurement

The particle image velocimetry (PIV) system was used to capture the flow dynamics in the wake of the submersible. As shown in Fig. 1, the PIV experiments were performed in the same recirculating water tank. A high-speed camera (FASTCAM_Mini_AX100) was employed, which offers a maximum resolution of 2048×2048 pixels and a maximum frame rate of 4000 fps. During the experiments, the camera was operated at a resolution of 1920×1080 pixels and a frame rate of 500 fps. A pulsed laser with a power of 5 W was used to generate a light sheet

with a thickness ranging from 0.5 to 2 mm; in this study, a thickness of 1.5 mm was selected. The tracer particles (Model 100063-1) had a nominal diameter of 20 μ m. Measurements were conducted in the x-y plane aligned with the flow direction.

3. Theoretical analyses

3.1 Numerical Simulation Theory

For incompressible viscous fluids, neglecting the thermal wake effects of the submersible eliminates the need for the energy equation, as the flow physics can be fully described by the conservation laws of mass and momentum (Chang et al., 2006). Consequently, the viscous flow field is commonly modeled using the Reynolds-Averaged Navier-Stokes (RANS) equations (Yakhot and Orszag, 1986).

The continuity equation for an incompressible fluid is:

$$\frac{\partial u_i}{\partial x_i} = 0 \tag{1}$$

Where u_i denotes the velocity component in the x_i -direction, and x_i represents the spatial coordinates.

Conservation of momentum equation:

$$f_i - \frac{1}{\rho} \frac{\partial p}{\partial x_i} + v \nabla^2 u_i = \frac{\partial u_i}{\partial t} + u_j \frac{\partial u_i}{\partial x_i}$$
 (2)

A variable decomposition technique is used by the RANS method to decompose the instantaneous physical quantities into two parts, time-averaged and pulsating values, i.e.

$$\Phi = \overline{\Phi} + \Phi' \tag{3}$$

$$\overline{\Phi} = \frac{1}{At} \int_{t}^{t+\Delta t} \Phi(t) dt \tag{4}$$

Here, Φ represents the instantaneous value of a physical quantity, $\overline{\Phi}$ denotes the time-averaged value, and $\Phi^{'}$ indicates the fluctuating component.

The time-averaged continuity equation and the Reynolds-averaged momentum equation are obtained by expressing the velocity and pressure fields in Equations (1) and (2) as the sum of their mean and fluctuating components.

$$\frac{\partial U_i}{\partial x_i} = 0 \tag{5}$$

Where U_i is the average velocity in m/s;

Momentum equation (Reynolds equation):

$$\frac{\partial U_i}{\partial t} + U_j \frac{\partial U_i}{\partial x_j} = F_i - \frac{1}{\rho} \frac{\partial P}{\partial x_i} + v \frac{\partial^2 U_i}{\partial x_j \partial x_j} + \frac{1}{\rho} \frac{\partial \left(-\rho \overline{u_i u_j}\right)}{\partial x_j}$$

$$\tag{6}$$

where P is the average pressure in Pa and $-\rho \overline{u_i u_j}$ is defined as the Reynolds stress.

3.2 Dynamic Modal Decomposition

The DMD method leverages time-series data to construct a low-dimensional representation of the system, enabling modal decomposition, dimensionality reduction, and simplification of the system dynamics through its characteristic modes.

The flow field data obtained from PIV measurements are processed to produce N snapshots captured at different time instances, which are arranged into the snapshot matrix $X_1^N = [x_1 \quad x_2 \quad \cdots \quad x_N]$. The time interval between consecutive snapshots is denoted as Δt . Subsequently, two derived snapshot matrices, $X_1 = [x_1 \quad x_2 \quad \cdots \quad x_{N-1}]$ and $X_2 = [x_1 \quad x_2 \quad \cdots \quad x_N]$, are constructed. Assuming a linear mapping A exists between X_1 and X_2 , viz.

$$X_2 = AX_1 \tag{7}$$

A locally linear dynamics is assumed by the linear approximation, which holds for weakly

nonlinear flows but may require higher-order corrections in strongly turbulent regimes.

Firstly, singular value decomposition (SVD) is applied to matrix X_1 to obtain the two matrices U and V and the diagonal array Σ :

$$X_1 = U \Sigma V^T \tag{8}$$

Next, the similarity matrix B of matrix A is obtained:

$$A \approx B = U^T Y V \Sigma^{-1} \tag{9}$$

The dominant eigenvalues of A are contained in B. Therefore, the eigenvalues of A can be estimated from those of B, and the resulting modal matrix is defined as Φ , whose columns represent the DMD modes:

$$\Phi = UW \tag{10}$$

Where *W* is the identity matrix corresponding to matrix B.

Thus, the flow field at any time can be reconstructed or predicted by:

$$X_i \approx \sum_{k=1}^r \Phi_k \left(\mu_k \right)^{i-1} \alpha_k \tag{11}$$

Where Φ_k represents the k-th DMD mode, μ_k denotes the k-th eigenvalue, and α_k is the amplitude of the k-th mode.

The mode energy is typically expressed as follows during the calculation:

$$||DM|| = |\lambda_m|^2 \tag{12}$$

Where λ_m is the complex eigenvalue of the *m*-th DMD mode, and $|\lambda_m|$ represents the modal length of the mode, indicating the degree of gain or decay.

Each DMD mode A is associated with a frequency B, which is related to the corresponding complex eigenvalue:

$$\lambda_m = \alpha_m + i\beta_m \tag{13}$$

Here, α_m is the decay rate of the mode and β_m is the oscillation frequency of the mode, with units of rad/s.

4. Results and discussion

4.1 Numerical simulation

The submersible model employed in this study is a simplified, scaled-down version of the Jiaolong submersible, as shown in Fig. 2(a). The model has a length L=220~mm and a maximum diameter D=60~mm, l denotes the length of the silk appendage. The numerical model matches the experimental setup at a 1:1 scale. To examine the flow field distribution characteristics of a conventional submersible, numerical simulations were carried out. A grid independence study was conducted at a flow velocity of 0.3 m/s prior to the simulation; the results are summarized in Table 1. Among these cases, the difference in the drag coefficient value between Case 4 and Case 5 is less than 1%. (Here, $C_D = \frac{2F_D}{\rho r^2 A}$, F_D is the drag force, ρ is the water density, ν is the flow velocity, and A is the maximum projected region of the submersible cross-section.) Based on these results, the grid configuration from Case 4 was selected for all subsequent simulations to achieve an optimal balance between computational accuracy and efficiency.

Furthermore, a time-step independence study was conducted to ensure the temporal accuracy of the unsteady simulations using the Case 4 mesh. The results are summarized in Table 2. The time-averaged drag coefficient (C_D) was monitored until a periodic steady state was achieved. As shown in Table 2, the difference in C_D between Case 3 and Case 4 is less than 0.5%, indicating that further time-step reduction has negligible impact on the solution. Thus, the time step from Case 3 was adopted for all subsequent transient simulations. The RNG k- ε model was employed as the turbulence model, as it better captures flows with adverse pressure gradients (Escue and Cui, 2010). Other simulation parameters are summarized in Table 3. Based

on these settings, Fig. 3 shows a schematic of the mesh domain and a close-up view of the computational mesh.

Figs. 4(a-e) show the distribution of turbulent kinetic energy (TKE) around the flow field of the submersible at different Reynolds numbers, with the isosurface level set at 0.2 TKEmax (where TKEmax denotes the maximum TKE in the flow field). TKE characterizes the intensity and energy of fluid turbulence, reflecting the energy distribution of velocity fluctuations and vortex structures. It can be observed that high-TKE regions are concentrated near the bow and stern across all Reynolds numbers. As the Reynolds number increases, the turbulence intensifies, indicating stronger vortex-dominated turbulence in these regions.

Figs. 5(a-e) show the pressure and vortex distributions in the flow field around the submersible at different Reynolds numbers, visualized using a Q-criterion value of 800 (isosurface). An adverse pressure gradient is evident in the amidships and stern regions across all Reynolds numbers. Consistent with previous studies (Tao et al., 2024; Perry et al., 1966a, 1966b), this adverse pressure gradient is linked to the transition from laminar to turbulent boundary layer in these areas. The adverse pressure gradient near the midsection and stern is identified as a dominant mechanism, as it promotes surface boundary layer separation and subsequent vortex formation in the wake. This observation provides the rationale for installing silk appendages specifically in these regions to alleviate the adverse pressure gradient and suppress flow separation. Additionally, vortex structures are predominantly concentrated in the bow and stern regions, typically resulting from flow separation, backflow, and vortices along the submersible surface. At elevated Reynolds numbers, the flow in these regions exhibits greater complexity, exhibiting more intricate vortex structures and higher vortex intensities.

Based on numerical simulation, a layered silk appendage arrangement strategy (320 denier, 1 denier = 1 g/9,000 m) is implemented on the submersible surface (Figs. 2 b-c). In the boundary layer control region, 16 silk appendage bundles (8 per side) are installed along the A-line in the amidships region to delay boundary layer separation by preemptively mitigating the adverse pressure gradient. In the wake control region, silk appendages are mounted along the B-line on both sides of the bow and stern (two bundles at the bow and three at the stern) to disrupt the wake vortex structure and improve wake characteristics. The physical parameters of the silk appendages are listed in Table 4.

4.2 Experimental analysis of drag force

To systematically evaluate the impact of silk appendages on submersible drag characteristics during vertical diving, controlled drag experiments were carried out with systematically varied silk appendage lengths. The experimental matrix (Table 5) comprised two variable groups: Group A and Group B, with length variations expressed in normalized form (l/L). Fig. 6 demonstrates the nonlinear relationship between normalized appendage length and drag coefficient (C_D). Experimental results align with the drag coefficient values predicted by CFD simulations for conventional submersibles in Tables 1 and 2, confirming the reliability of the CFD modeling. Both sets of silk appendages exhibit a characteristic "valley-shaped" trend, where the drag coefficient first decreases and then increases with normalized silk appendage length. The initial decrease in drag is attributed to the effective stabilization of the flow field by the silk appendages. At their optimal lengths (A=0.05 L, B=0.2 L), the silk appendages function as passive flow control devices. They penetrate the boundary layer, accelerating momentum exchange, a process that attenuates adverse pressure gradients, thereby suppressing

boundary layer separation. Consequently, the pressure drag component induced by separation is reduced. Conversely, excessively long silk appendages (e.g., A=0.15 *L*) begin to adversely affect the flow. Their length and flexibility enable more vigorous interaction with high-momentum outer flow regions. This intense interaction introduces additional oscillations and large-amplitude flapping motions, which exacerbate flow instabilities and turbulence generation within the boundary layer and wake.

The present study reveals a notable interdependence between the silk appendages of Groups

A and B. As the length of the Group B appendages is varied, the Group A appendages consistently exhibit a similar "valley-shaped" trend in the drag coefficient (C_D) . Among these configurations, the case where both Group A and Group B have a silk appendage length of zero represents the conventional submersible, serving as the control group for this experiment, with a drag coefficient of 0.8543. Group A achieved optimal drag reduction at l/L = 0.05, while Group B reached its optimum at l/L = 0.2. The corresponding drag coefficient for this combined optimal configuration was 0.7973, yielding a maximum drag reduction rate of 6.67% (± 0.3 %). According to the analysis shown in Fig. 6, variations in the length of Group A silk appendages significantly influence the relationship between the silk appendage length in Group B and the resulting submersible drag. The drag reduction effect observed in Section 4.2 motivates further investigation into the underlying flow mechanisms, as analyzed below. To simplify the presentation of operating conditions, four cases are specified. Case (a): Group A and Group B silk appendage lengths are 0 (A=0 L, B=0 L). Case (b): l/L = 0 for group A and l/L = 0.2 for group B (A=0 L, B=0.2 L). Case (c): Group A silk appendage length is l/L = 0.05, and group B silk appendage length is l/L = 0.2 (A=0.05 L, B=0.2 L). Case (d): Group A silk

appendage length is l/L = 0.15, and group B silk appendage length is l/L = 0.2 (A=0.15 L, B=0.2 L). All subsequent flow field studies are conducted under these four operating conditions.

4.3 Flow field structure analysis

4.3.1 Time averaged flow field

Fig. 7 shows the normalized time-averaged streamlines and vorticity cloud maps for submersibles with different silk appendage lengths. For A=0 L, B=0 L (Fig. 7 a), pairs of distinct large-scale vortices with high vortex strength are observed in the bow and stern regions. This aligns with the vortex structure predicted by numerical simulations for conventional submersibles (Fig. 5c), further validating the reliability of the CFD results. This suggests that intense fluid motion occurs in these regions, leading to an unstable flow field. For A=0 L, B=0.2 L (Fig. 7b), the large-scale vortex structure in the wake are reduced, confirming the effectiveness of installing silk appendages within the wake control zone (B-line). This indicates that the incorporation of silk appendages improves the flow around the submersible, allowing the fluid to adhere more effectively to its surface. For A=0.05 L, B=0.2 L (Fig. 7c), the largescale vortex structures in the bow and stern are displaced farther from the submersible. This shows that the Group A silk appendages at an optimal length (1/L=0.05) effectively suppress boundary layer separation induced by the adverse pressure gradient. For A=0.15 L, B=0.2 L (Fig. 7d), vorticity intensifies throughout the flow field, likely resulting from excessive appendage length amplifying separation within the boundary layer and promoting stronger vortex formation.

Fig. 8 shows the normalized root-mean-square (RMS) velocity distributions for submersibles with different silk appendage lengths. (The first and second-order turbulence statistics are

normalized by U and U^2 , respectively, where U is the free stream velocity.) For A=0 L, B=0 L (Fig. 8a), a pronounced low-speed region appears in the wake, extending from X/L=0.1 to 0.9, which corresponds to the vortical region shown in Fig. 7(a). For Figs. 8(b-c), both the high-speed region in the wake and the low-speed region near the midship are reduced, primarily owing to the influence of the Group B silk appendages. The suppression of the low-speed region also indicates that the Group A silk appendages mitigate boundary layer separation. Together, these modifications contribute to decreased vortex intensity and improved flow stability. For A=0.15 L, B=0.2 L (Fig. 8d), the high-speed region in the bow wake expands, while the low-speed region amidships remains largely unaffected. This suggests that the longer Group A silk appendages enhance flow acceleration near the bow. However, the increased complexity of flow disturbances in the midship region may aggravate boundary layer separation and vortex formation, thereby increasing flow field instability.

Fig. 9 shows the normalized Reynolds stress distribution for the submersible with different silk appendage lengths. For A=0 L, B=0 L (Fig. 9a), distinct high-Reynolds-stress regions are present at both the bow and stern. Positive Reynolds stress indicates the transverse expansion of turbulence, reflecting intense turbulent motion in the bow region. Negative Reynolds stress represents the transverse compression of turbulence, suggesting that turbulent kinetic energy in the stern region tends to concentrate near the submersible surface. For the silk appendage submersible (Figs. 9b-d), the area of positive Reynolds stress in the bow wake is reduced, indicating that the silk appendage suppress turbulent expansion and foster a more stable flow. Conversely, the region of negative Reynolds stress in the stern gradually increases and expands toward the bow, indicating that as flow separation is reduced, turbulence intensity in the stern

increases, enhancing the agglomeration of turbulence along the submersible surface, which extends toward the bow.

Fig. 10 shows the normalized turbulent kinetic energy (TKE) distribution for submersibles with different silk appendage lengths. For $A=0\,L$, $B=0\,L$ (Fig. 10a), a large high-TKE region is observed in the flow field around the submersible, extending from the bow to the stern. This indicates that the flow field is highly turbulent, likely due to the intensification of turbulence caused by flow separation at the bow. The flow velocity at the bow varies significantly, producing a strong velocity gradient that, in turn, promotes vortex formation. After silk appendages are added (Fig. 10b-d), the high TKE regions in the flow field are reduced to varying degrees, and the TKE distribution becomes more organized. This reduction in TKE is a direct consequence of the suppression of boundary layer separation—attributed to the Group A silk appendages—and the optimization of the wake structure, resulting from the Group B silk appendages.

4.3.2 Transient flow field

In this study, 7,198 flow field snapshots were continuously captured over a 14.4-second duration using a high-speed camera. The normalized instantaneous streamline distributions of the submersible with different silk appendage lengths at t = 7 s are shown in Fig. 11. For A=0 L, B=0 L (Fig. 11a), distinct vortex structures are observed at (X/L = 0.4, Y/L = 0.1) and (X/L = 0.2, Y/L = 0.9). These vortices indicate intense periodic vortex shedding, which constitutes the primary source of pressure drag. For A=0 L, B=0.2 L (Fig. 11b), the vortex at the bow is shifted towards the midship. More significantly, the vortex structure at the stern is disrupted and fragmented into smaller scales by the action of the Group B silk appendages, indicating

that the silk appendages effectively break up the primary large-scale vortices responsible for high drag. In contrast, with the addition of Group A silk appendages (Figs. 11 c-d), the vortex at the bow gradually intensifies, while the vortex at the stern is displaced farther from the submersible surface, indicating that longer silk appendages exert a stronger influence on flow separation, thereby amplifying its effect on the flow field.

Fig. 12 shows the fluctuation intensity profiles along the y-direction at X/L = 0.3 for submersibles with different silk appendage lengths. The fluctuation intensity $I_u = \left(u_p^{-2} + v_p^{-2}\right)/U^2$ is a dimensionless value, where u_p' is the fluctuating velocity in the x-direction, v_p' represents the fluctuating velocity in the y-direction, and U is the average flow velocity. For A=0 L, B=0 L (Fig. 12a), distinct peaks are shown in the pulsation intensity fluctuation curve at Y/L = 0.1095 and 0.7808, corresponding to the vortex positions in the submersible wake shown in Fig. 11. After silk appendages are introduced (Figs. 12b-d), the fluctuation intensity is significantly attenuated. This shows that vortex-induced unsteadiness in the wake region is suppressed by the silk appendages. However, in Figs. 12(b-c), the peak fluctuation intensity in the stern region is decreased, whereas in Fig. 12(d), it is increased. These changes suggest that although the silk appendages generally improve the flow characteristics, the long Group A silk appendages enhance boundary layer separation, leading to a localized increase in fluctuation intensity.

4.4 Time-frequency analysis

The continuous wavelet transform (CWT) is widely used in time-frequency analysis of signals as it provides local characteristics in both the time and scale domains. To investigate the time-frequency characteristics of the submersible wake field before and after the addition of silk appendage, the Mexican Hat wavelet was employed in this study to perform CWT

analyze at two specific points within the vortex: (X/L = 0.3, Y/L = 0.1) and (X/L = 0.3, Y/L = 0.9). Time-frequency contour plots were generated, and the corresponding fluctuating velocity-time variations for these two points are displayed below the plots.

The time-frequency distribution in the x-direction of the submersible wake field at (X/L = 0.3, Y/L = 0.1) is shown in Fig. 13. Near the dominant frequency of 0.13897 Hz, a series of alternating positive and negative red and blue stripes are observed, indicating that periodic "large-scale" flow oscillations are present in the submersible flow field (Ozgeren, 2006). The red and blue stripes represent the positive and negative phases of the velocity fluctuations, respectively. In the relatively high-frequency range (0.3 Hz < f < 10 Hz), multiple stripes are also discernible, indicating that presence of relatively "small-scale" vortical structures. The dense distribution of these high-frequency components implies strong activity of localized turbulence or small-scale vortices in the flow field (Zheng et al., 2020). In Figs. 13(b - d), the frequency of alternating positive and negative stripes in the large-scale flow field decreases, while their temporal width increases, indicating that the periodic oscillation of large-scale vortices and disturbances is slowed. Conversely, the time-frequency distribution of the small-scale flow field becomes denser, reflecting an increase in high-frequency components. This further confirms that the silk appendages activate relatively small-scale vortical structures.

Fig. 14 shows the time-frequency distribution characteristics in the y-direction at (X/L = 0.3, Y/L = 0.1) in the flow field of the submersible with different silk appendage lengths. Compared with the time-frequency distribution characteristics in the x-direction shown in Fig. 13, the intensity of the fluctuations in the y-direction is significantly lower. This indicates that, in the flow field around the submersible, velocity fluctuations are more pronounced in the x-direction,

while disturbances in the y-direction are relatively weak. This constitutes a fundamental manifestation of turbulence anisotropy within the boundary layer and the wake (Nelkin, 2005). The stronger disturbance in the x-direction is a characteristic phenomenon behind the blunt body, where primary flow separation and vortex shedding are governed by flow-induced momentum waves. In addition, coupling between the flow field fluctuations in the x- and y-directions is observed. This coupling promotes the redistribution of turbulent kinetic energy between the two directions, serving as the primary mechanism for energy transfer among velocity components.

The time-frequency distribution characteristics in the x- and y-directions within the submersible wake field at (X/L = 0.3, Y/L = 0.9) under different operating conditions are shown in Figs. 15 and 16. In Figs. 15(b-c) and 16(b-c), after silk appendages are introduced, the fluctuation amplitude in both the x-direction and y-direction decreases. This indicates that the silk appendages suppress irregular vortex fluctuations, thereby reducing turbulent mixing and momentum loss, which directly contributes to drag reduction. However, as the length of the silk appendage increases further, the amplitude of the velocity fluctuations in both directions also increases, as shown in Figs. 15(d) and 16(d). This behavior is consistent with the time-frequency characteristics observed at (X/L = 0.3, Y/L = 0.1). These results demonstrate that the stability of the flow field is closely related to the length of the silk appendage. Silk appendages of appropriate length are shown to enhance flow field stability by facilitating the breakdown of large-scale vortices into small-scale structures while suppressing vortex-induced velocity fluctuations. However, as the silk appendage length increases, this beneficial effect diminishes.

4.5 DMD analysis on flow fields

Time-frequency analysis using CWT reveals that silk appendages induce a transition in vortex dynamics: large-scale periodic flows are suppressed, while small-scale vortex structures are activated. This energy shift from large-scale to small-scale vortices aligns with the principles of the turbulence energy cascade (Kolmogorov, 1941), a fundamental process in turbulent flows whereby energy is transferred from larger eddies to smaller ones until it is dissipated viscously at the Kolmogorov scale. The suppression of low-frequency modes (large-scale structures) and the concomitant enhancement of high-frequency modes (small-scale structures) indicate that the silk appendages promote a more efficient energy cascade. By breaking down large coherent vortices into smaller, more dissipative structures, the silk appendages facilitate a quicker energy dissipation pathway, thereby reducing the overall turbulent kinetic energy and enhancing flow stability. This mechanism contributes directly to drag reduction. To quantitatively corroborate this energy redistribution mechanism, Dynamic Mode Decomposition (DMD) is employed to decompose the flow field into dominant frequency modes and analyze the modal-scale energy transfer.

Fig. 17 shows the energy distribution and energy accumulation curves for the first 10 DMD modes for submersibles with varying silk appendage lengths. The modal energy decreases progressively across all test cases, and the rate of increase of the energy accumulation curve gradually slows. Lower-order modes may not fully capture the flow field characteristics; therefore, increasing the modal order significantly enhances the cumulative energy representation. By the 10th mode, the cumulative energy values for Figs. 17(a-d) are 97.488%, 89.506%, 86.951%, and 91.607%, respectively, indicating that the DMD mode up to this order provide a sufficiently complete representation of the flow field. Furthermore, after the addition

of silk appendages (Figs. 17 b-d), the cumulative energy of the first 10 DMD modes decreases to varying degrees, reflecting a reduction in the energy concentration within the dominant modes. This energy redistribution suggests a suppression of energetic structures linked to boundary layer separation (addressed by Group A appendages) and large-scale wake vortices (controlled by Group B appendages). The resulting enhancement of flow stability is a direct consequence of this suppression, along with the concomitant promotion of small-scale vortical activity.

Fig. 18 shows the relationship between the DMD modal energy ||DM|| of each mode on the xy-plane and the corresponding frequency f, obtained by transforming $f = \frac{\text{Im}\{\log(\lambda_i)\}}{2\pi\Delta t}$ for submersibles with varying silk appendage lengths. As shown in the figure, high modal energy values are primarily concentrated in the low-frequency range (f < 5.8 Hz), indicating that the dynamic characteristics of the submersible flow field are predominantly governed by low-frequency modes. Primary and secondary peaks are observed at frequencies of f = 0.138 Hz and f = 8.891 Hz, respectively. Compared with condition (a), the amplitudes of the main and secondary peaks in conditions (b-d) were significantly reduced when silk appendages were added. This reflects the weakening of large-scale vortex motions due to the combined effect of the Group A and Group B silk appendages. The concurrent rise in modal energy at higher frequencies (f > 30 Hz) supports the notion that energy is transferred to smaller scales, which is characteristic of an optimized wake structure in which turbulent energy is dissipated more efficiently, thereby contributing to drag reduction.

Fig. 19 shows the time-coefficient spectra of each mode of the submersible, obtained by performing a fast Fourier transform (FFT). The highest energy occurs at f = 0.13897 Hz,

demonstrating the capability of dynamic mode decomposition to extract flow structures at specific scales (Yan et al., 2025b). The corresponding Strouhal number ($St=\frac{fL}{U}$) is 0.1019, indicating that periodic vortex shedding occurs in the flow field of the submersible, which is considered a typical feature of turbulence in the wake of a blunt body (Hussain et al., 1983). Compared to the conventional submersible (Fig. 19a), the energy amplitudes of the time coefficients decrease by 14.54%, 9.36%, and 2.52%, respectively, after the addition of the silk appendage (Figs. 19 b-d), and the decreasing trend in energy amplitudes gradually weakens. This phenomenon may be attributed to two factors: on the one hand, as the silk appendage length increases, the boundary layer thickness near the surface also increases, causing boundary layer stability to approach its limit and the near-surface flow perturbations to become more complex (Ramaswamy et al., 2024). On the other hand, the damping effect of the silk appendages, although effective in suppressing vibrations, tends to saturate with increasing length, leading to a gradual reduction in their ability to inhibit large-scale flow features.

Fig. 20 shows the reconstruction results of the normalized velocity field for the dominant mode ($f = 0.13897 \ Hz$), obtained using the DMD method for submersibles with different silk appendage lengths. For A=0 L, B=0 L (Fig. 20a), a large-scale, high-velocity flow region is formed near the bow of the submersible, while a significant backflow region appears amidships. This indicates that kinetic energy is primarily concentrated in the large-scale flow structures. For Figs. 20 (b-c), the rearward shift of the high-speed flow region and the pronounced weakening of the midship backflow clearly demonstrate the suppression of boundary layer separation achieved by the Group A silk appendages. Conversely, excessively long Group A silk appendages (Fig. 20 d) fail to suppress separation and instead induce stronger backflow

regions amidships and near the stern, clearly illustrating the detrimental effect of improper silk appendage length on boundary layer control and flow stability.

Fig. 21 shows the distribution of the real and imaginary parts of the eigenvalues of the DMD modes on the unit circle for submersibles with different silk appendage lengths. In this representation, points located inside the unit circle indicate a stable mode, while points on the unit circle correspond to marginal stability. The four operating conditions are all observed to exhibit decaying behavior. Fig. 22 shows the relationship between the decay rate and frequency of the DMD modes. The discrete points in the decay rate-frequency plot correspond to the eigenvalues on the unit circle, with darker colors indicating higher modal energy and lighter colors representing lower energy. Most discrete points are concentrated in the critically stable periodic and damped regimes, with only a few located in weakly unstable periodic modes. For Fig. 22(b) and Fig. 22(c), the decay rates of all discrete points are concentrated between -15 and 5, exhibiting a relatively compact distribution. This shows that after the addition of silk appendages, the decay characteristics of the system modes become more consistent, highlighting the effectiveness of the silk appendages in suppressing modal divergence and enhancing flow field stability. In contrast, for Fig. 22(a) and Fig. 22(d), some low-energy points display decay rates exceeding -15, and the distribution of points is more scattered. This indicates that both the absence of silk appendages and the use of excessively long silk appendages lead to increased complexity and instability in the flow field, thereby reducing their ability to suppress large-scale vortical structures.

5. Conclusion

To investigate the drag reduction mechanism of double-row silk appendages on submersibles,

experiments were conducted using torque sensors and particle image velocimetry. The results are analyzed in terms of time-averaged flow field, instantaneous flow field, time-frequency analysis, and dynamic modal decomposition. The main findings are summarized as follows:

- (1) The installation of double-row silk appendages significantly reduces the drag of the submersible. The optimal configuration (A=0.05 L, B=0.2 L) achieves a maximum drag reduction rate of 6.67% ($\pm 0.3\%$). Time-averaged and transient flow field analyses confirm that the silk appendages effectively suppress boundary layer separation and disrupt large-scale vortex structures in the wake.
- (2) The silk appendages suppress boundary layer separation induced by adverse pressure gradients, particularly in the midsection and stern regions. They promote the breakdown of large-scale vortices into smaller-scale structures, as evidenced by time-frequency analysis using CWT. DMD reveals a redistribution of modal energy from large-scale to small-scale modes, enhancing energy dissipation and flow stability. However, excessively long appendages (e.g., A=0.15 L, B=0.2 L) may amplify local disturbances and destabilize the flow.
- (3) The double-row layout (Group A for boundary layer control, Group B for wake optimization) provides an effective passive drag reduction strategy. The silk appendage length ratio (l/L) should be carefully selected to balance vortex suppression and flow stability. This study demonstrates the potential of silk appendages in enhancing the hydrodynamic performance of underwater vehicles.

6. Limitations and Outlook

This study provides insights into the drag reduction mechanism of silk appendages; however, several limitations should be noted. Firstly, the underwater model used in this study is

considerably smaller than full-scale submersibles, and the Reynolds number at the experimental flow velocity (Re=65,749) is lower than that in encountered in actual deep-sea operating conditions (typically $Re>10^6$). As a result, the direct applicability of the current findings to other submersibles may be limited. The drag reduction mechanism identified in this study relies primarily on the modulation of vortex structures. The effect of silk appendages on frictional drag under higher Reynolds number conditions requires further evaluation.

Additionally, due to limitations in the experimental setup and funding, the current PIV measurements are restricted to two-dimensional (2D) flow fields within a single plane (x-y). Although this approach captures representative wake structures and their modifications, it does not fully capture the three-dimensional (3D) nature of vortex dynamics.

To address these limitations, future work will focus on the following aspects: conducting high-Reynolds-number experiments using larger-scale models to better simulate deep-sea hydrodynamic environments, along with optimized experimental designs; employing advanced flow diagnostic techniques, such as stereo-PIV, to characterize 3D wake structures and quantify out-of-plane vorticity components, thereby validating the quasi-2D assumptions adopted in this study and elucidating the 3D interactions between appendages and turbulent wakes; systematically evaluating the performance of different flexible appendage materials to enhance the generalizability of the conclusions; and leveraging Dynamic Mode Decomposition (DMD) results to correlate geometric parameters of silk appendages with flow modes, facilitating optimized structural designs that suppress key instabilities specific to submersible configurations.

Acknowledgments

The author wishes to acknowledge the support given to him by the Major Basic Research Project of the Natural Science Foundation of the Jiangsu Higher Education Institutions of China (24KJA130001).

Reference

- [1] DU M., PENG X., ZHANG H., et al., 2021. Geology, environment, and life in the deepest part of the world's oceans. The Innovation, 2(2), 1-11. https://doi.org/10.1016/j.xinn.2021.100109
- [2] ZHAI X., ZHANG H., WANG S., et al., 2024. Experimental study on the drag reduction of underwater vehicles by drag-reducing agents injection. Applied Ocean Research, 153, 104303. https://doi.org/10.1016/j.apor.2024.104303
- [3] CHEN, L., LIU, S., & ZHAO, J. L. Y. . 2022. Stability and drag reduction in turbulent flow of skin with quasi-periodic elastic supports. Proceedings of the Institution of Mechanical Engineers, Part M. Journal of Engineering for the Maritime Environment, 236(4), 1057-1068. https://doi.org/10.1177/14750902221076239
- [4] LI, S., LIU, S., ZHAO, D., et al., 2024. Drag reduction characteristics of the placoid scale array skin sup-ported by micro stewart mechanism based on penalty immersed boundary method. Applied Ocean Research, 149. https://doi.org/10.1016/j.apor.2024.104049
- [5] XIE W., LUO Z., ZHOU Y., et al., 2021. Experimental and numerical investigation on opposing plasma synthetic jet for drag reduction. Chinese Journal of Aeronautics, 35(8), 75-91. https://doi.org/10.1016/j.cja.2021.10.027
- [6] LUO Y., WANG L., GREEN L., et al., 2015. Advances of drag-reducing surface technologies in turbulence based on boundary layer control. Journal of Hydrodynamics, 27(4), 473 487. https://doi.org/10.1016/S1001-6058(15)60507-8
- [7] MONFARED MOSGHANI M., ALIDOOSTAN M.A., BINESH A., 2023. Numerical analysis of drag reduction of fish scales inspired Ctenoid-shape microstructured surfaces.

- Chemical Engineering Communications, 210(6), 970-985. https://doi.org/10.1080/00986445.2021.1992398
- [8] DURBIN P., WU X.H., 2007. Transition beneath vortical disturbances. Annual Review of Fluid Mechanics, 39(1), 107-128. https://doi.org/10.1146/annurev.fluid.39.050905.110135
- [9] CUI W., WANG F., PAN B., et al., 2015. Issues to be solved in the design, manufacture and maintenance of a full ocean depth manned cabin. Advances in Engineering Research, 1(1), 1–29.
- [10] SU Y.M., CHEN Q.T., SHEN H.L., et al., 2012. Numerical simulation of a planing vessel at high speed. Journal of Marine Science and Application, 11(2), 178-183. https://doi.org/10.1007/s11804-012-1120-7
- [11] NOURI A., DEMIM F., NEMRA A., 2024. 3D Simulation of Appendage Effect on the submersible Drag. Unmanned Systems, 12(6), 1039-1062. https://doi.org/10.1142/S2301385024500365
- [12] AHMAD H., BAIG M.F., FUAAD P.A., 2015. Numerical investigation of turbulent-drag reduction induced by active control of streamwise travelling waves of wall-normal velocity. European Journal of Mechanics B/Fluids, 49, 250-263. https://doi.org/10.1016/j.euromechflu.2014.09.004
- [13] GAO S., PAN S., WANG H.C., TIAN X.L., 2020. Shape Deformation and Drag Variation of a Coupled Rigid-silk System in a Flowing Soap Film. Physical Review Letters, 125(3), 034502. https://doi.org/10.1103/PhysRevLett.125.034502
- [14] TIAN X.L., 2021. silk Coating Reduces Drag. Journal of Shanghai Jiao Tong University,

- 55(2), 213-214. https://xuebao.sjtu.edu.cn/EN/10.16183/j.cnki.jsjtu.2020.393
- [15] MAO Q., LIU Y., SUNG H.J., 2023. Drag reduction by flapping a pair of silk filaments behind a cylinder. Physics of Fluids, 35(3), 034122. https://doi.org/10.1063/5.0101446
- [16] YAN F., ZHANG G.Q., RINOSHIKA A., et al., 2025. A study on the wake structure of an ascending submersible with silk silk appendages using continuous wavelet transform and dynamic mode decomposition. Experimental Thermal and Fluid Science, 160, 111323. https://doi.org/10.1016/j.expthermflusci.2024.111323
- [17] YAN F., KONG W.Y., RINOSHIKA A., et al., 2025. Analyses on flow structures behind submersible with silk appendage during floating based on continuous wavelet transform and dynamic mode decomposition. Applied Ocean Research, 154, 104397. https://doi.org/10.1016/j.apor.2024.104397
- [18] TAO Z., MA Y., YOU R.Q., et al., 2024. A review of the research progress of boundary layer theory (in Chinese). Scientia Sinica Technologica, 54, 979-1002. https://doi.org/10.1360/SST-2023-0316
- [19] PERRY A.E., BELL J.B., JOUBERT P.N., 1966. Velocity and temperature profiles in adverse pressure gradient turbulent boundary layers. Journal of Fluid Mechanics, 25(2), 299-320. https://doi.org/10.1017/S0022112066001666
- [20] PERRY A.E., 1966. Turbulent boundary layers in decreasing adverse pressure gradients.

 Journal of Fluid Mechanics, 26(3), 481-550. https://doi.org/10.1017/S0022112066001344
- [21] TANARRO A., VINUESA R., SCHLATTER P., 2019. Effect of adverse pressure gradients on turbulent wing boundary layers. Journal of Fluid Mechanics, 883, A25. https://doi.org/10.1017/jfm.2019.838

- [22] NGUYEN T.P., NGUYEN Q.V., NGUYEN V.H., et al., 2019. Silk fibroin-based biomaterials for biomedical applications: a review. Polymers, 11(12), 1933. https://doi.org/10.3390/polym11121933
- [23] VEPARI C., KAPLAN D.L., 2007. Silk as a biomaterial. Progress in Polymer Science, 32(8-9), 991-1007. https://doi.org/10.1016/j.progpolymsci.2007.05.013
- [24] WANG C., XIA K., ZHANG Y., et al., 2019. Silk-Based Advanced Materials for Soft Electronics. Accounts of Chemical Research, 52(10), 2916-2927. https://doi.org/10.1021/acs.accounts.9b00333
- [25] ZHANG Y., LU H., LIANG X., et al., 2021. Silk Materials for Intelligent Fibers and Textiles: Potential, Progress and Future Perspective. Acta Physico-Chimica Sinica, 37(5), 2103034. https://doi.org/10.3866/PKU.WHXB202103034
- [26] ZHANG J., MAXWELL J.A., GERBER A.G., et al., 2013. Simulation of the flow over axisymmetric submersible hulls in steady turning. Ocean Engineering, 57, 180-196. https://doi.org/10.1016/j.oceaneng.2012.09.016
- [27] BOE C., RODRIGUEZ J., PLAZOLA C., et al., 2013. A hydrodynamic assessment of a remotely operated underwater vehicle based on computational fluid dynamic part 1 numerical simulation. Computer Modeling in Engineering & Sciences, 90(2), 165-193. https://doi.org/10.3970/cmes.2013.090.165
- [28] CHEN K.K., TU J.H., ROWLEY C.W., 2012. Variants of dynamic mode decomposition: boundary condition, koopman, and fourier analyses. Journal of Nonlinear Science, 22(6), 887-915. https://doi.org/10.1007/s00332-012-9130-9
- [29] LI S., LI F., HUANG Q., et al., 2023. On the space-time decomposition and reconstruction

- of the pump-jet propulsor flow field. Ocean Engineering, 286(Pt. 2), 115521. https://doi.org/10.1016/j.oceaneng.2023.115521
- [30] SONG Y., MING P., YU G., 2023. Research on unsteady characteristics of different appendaged submersibles flows based on dynamic mode decomposition. Ocean Engineering, 276, 114189. https://doi.org/10.1016/j.oceaneng.2023.114189
- [31] FARGE M., SCHNEIDER K., KEVLAHAN N., 1999. Non-gaussianity and coherent vortex simulation for two-dimensional turbulence using an adaptive orthogonal wavelet basis. Physics of Fluids, 11(8), 2187-2201. https://doi.org/10.1063/1.870080
- [32] ZHAO M., CHENG L., AN H., 2012. Numerical investigation of vortex-induced vibration of a circular cylinder in transverse direction in oscillatory flow. Ocean Engineering, 41, 39-52. https://doi.org/10.1016/j.oceaneng.2011.12.017
- [33] CHANG Y., ZHAO F., ZHANG J., et al., 2006. Numerical simulation of internal waves excited by a submersible moving in the two-layer stratified fluid. Journal of Hydrodynamics, 18(Suppl. 3), 330-336. https://doi.org/10.1016/S1001-6058(06)60074-7
- [34] YAKHOT V., ORSZAG S.A., 1986. Renormalization group analysis of turbulence. I. Basic theory. Journal of Scientific Computing, 1(1), 3–51 https://doi.org/10.1007/BF01061452
- [35] ESCUE A., CUI J., 2010. Comparison of turbulence models in simulating swirling pipe flows. Applied Mathematical Modelling, 34(10), 2840-2849. https://doi.org/10.1016/j.apm.2009.12.018
- [36] OZGEREN M., 2006. Flow structure in the downstream of square and circular cylinders.

 Flow Measurement and Instrumentation, 17(4), 225-235.

- https://doi.org/10.1016/j.flowmeasinst.2005.11.005
- [37] ZHENG Y., RINOSHIKA H., ZHANG D., RINOSHIKA A., 2020. Analyses on flow structures behind a wavy square cylinder based on continuous wavelet transform and dynamic mode decomposition. Ocean Engineering, 216, 108117. https://doi.org/10.1016/j.oceaneng.2020.108117
- [38] NELKIN, M. . 2005. Turbulence: an introduction for scientists and engineers. Physics Today, 58(10), 80-83. https://doi.org/10.1063/1.2138427
- [39] KOLMOGOROV, A., N. 1941. The local structure of turbulence in incompressible viscous fluid for very large reynolds numbers. Proceedings of the Royal Society A: Mathematical, 434, 9-13. https://doi.org/10.1098/rspa.1991.0075
- [40] HUSSAIN A. K. M. F., 1983. Coherent structures—reality and myth. Physics of Fluids, 26(10), 2816-2850. https://doi.org/10.1063/1.864048
- [41] RAMASWAMY V., NAMUROY C. M., HARRIS W. L., et al., 2024. Ultraspherical polynomial spectral method for boundary layer stability problems. Proceedings of the AIAA Aviation Forum and Ascend 2024, American Institute of Aeronautics and Astronautics, paper 3531. https://doi.org/10.2514/6.2024-3531

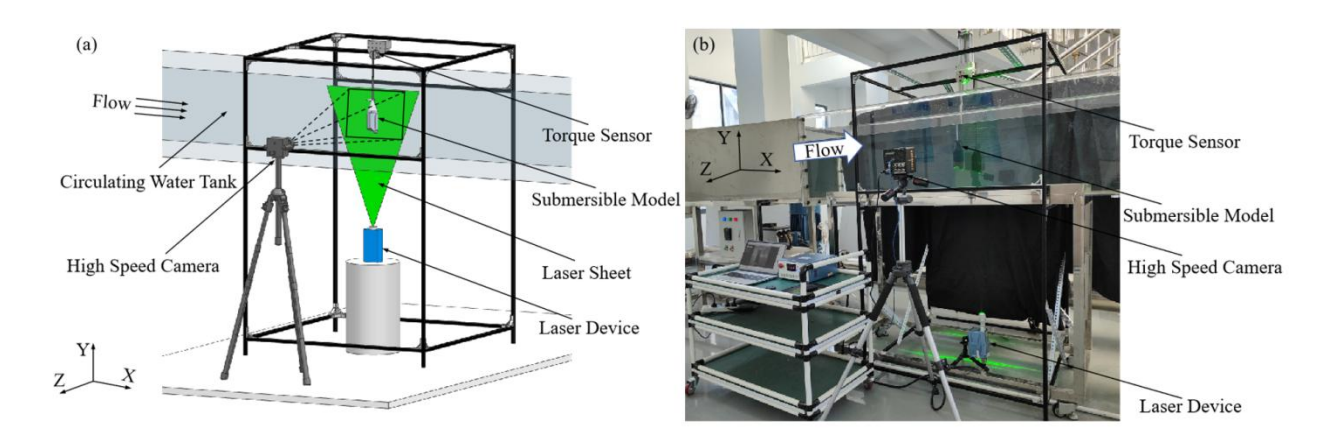


Fig. 1 Diagram of the Experimental Setup: (a) Schematic diagram of the setup. (b) Physical drawing of the experimental configuration.

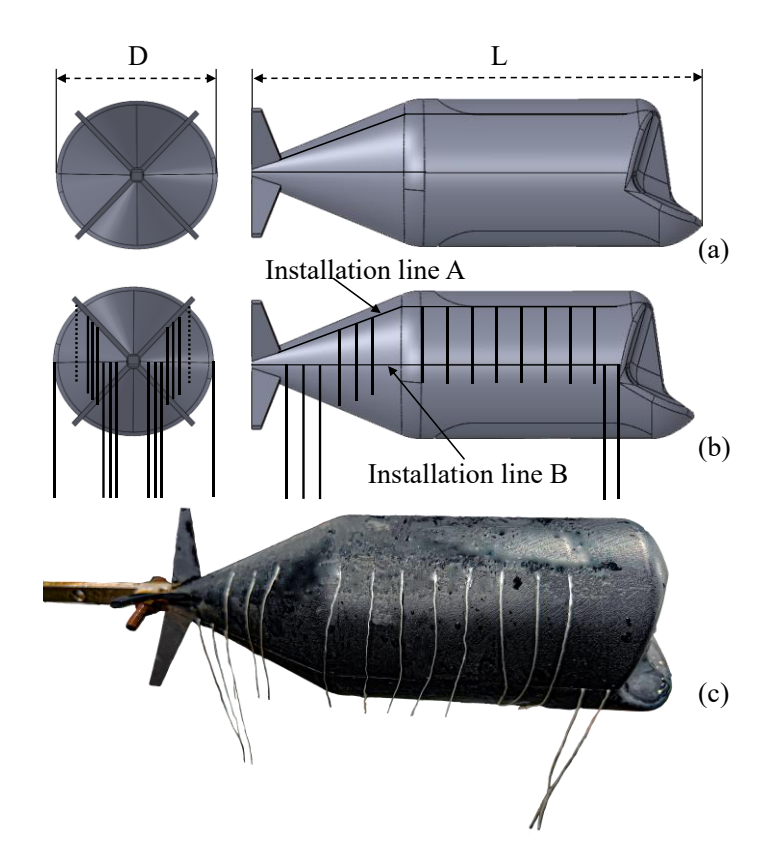


Fig. 2 Conventional submersible and silk silk appendage installation display. (a)

Conventional submersible. (b) Silk silk appendage installation location. (c) Physical drawing of silk silk appendage submersible installation.

Case	Number of grids	Drag	Drag coefficient	Relative error
		(F_D)	$\binom{C_D}{C_D}$	
1	2×10 ⁶	0.4716	0.8976	\
2	2.5×10^{6}	0.4633	0.8614	4.032%
3	3×10 ⁶	0.4623	0.8339	3.192%
4	3.5×10^{6}	0.4612	0.8465	1.511%
5	4×10 ⁶	0.4617	0.8514	0.057%

 Table 1. Validation of mesh-independence for numerical simulations.

Case	Time Step Δt (s)	Drag (FD)	Drag coefficient $\binom{C_D}{C}$	Relative Error
1	0.002	0.4751	0.8721	\
2	0.001	0.4658	0.8549	1.97%
3	0.0005	0.4620	0.8478	0.83%
4	0.00025	0.4605	0.8452	0.31%
5	0.0001	0.4598	0.8439	0.15%

Table 2. Time-step independence verification for numerical simulations.

Parameter	Value	
Reynolds Numbers (Re)	21,916, 43,948, 65,749, 87,666, 109,582	
Control Equation	RANS (Reynolds - Averaged Navier - Stokes)	
Convergence Criteria	1×10^{-5} (residuals)	
Flow Type	Turbulent	
y +	1.02	
Boundary Conditions	No-slip wall, Speed Inlet, Pressure outlet	
Grid Type	Unstructured grid	
Near-Wall Treatment	Enhanced wall treatment	
Number of Layers	15	

Table 3. Numerical simulation setup parameters.

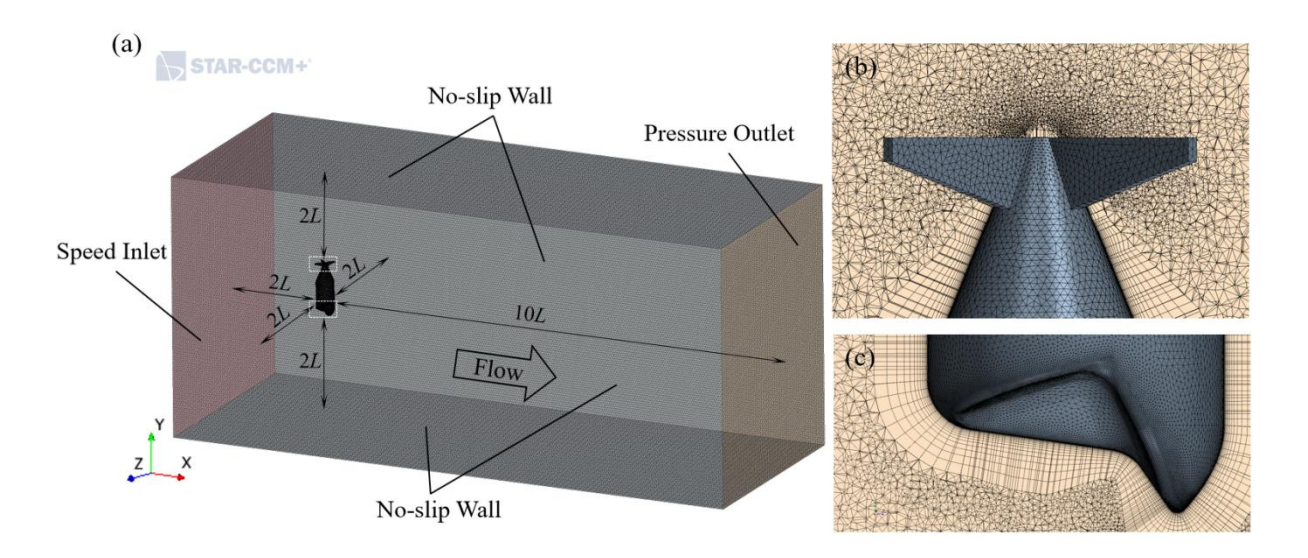


Fig. 3 Computational grid schematic diagram. (a) Computational domain grid; (b) Local enlargement of the submersible bow grid; (c) Local enlargement of the submersible stern grid.

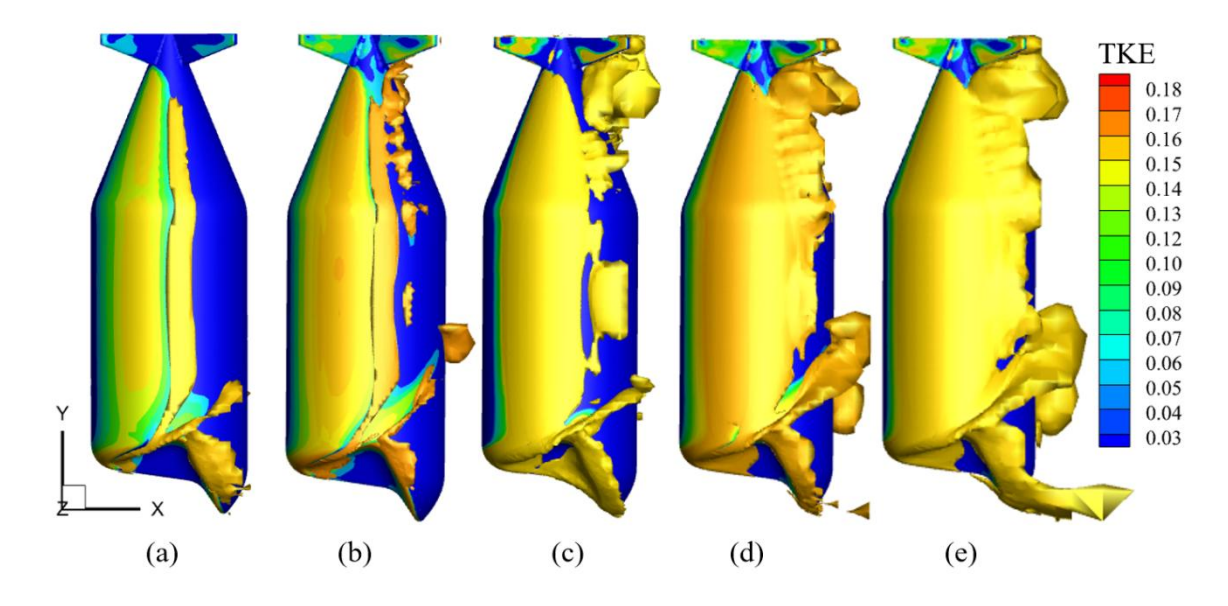


Fig. 4 The distributions of turbulent kinetic energy (TKE) in the flow field around the submersible for different Reynolds numbers. (a) Re=21,916 (b) Re=43,948 (c) Re=65,749 (d) Re=87,666 (e) Re=109,582.

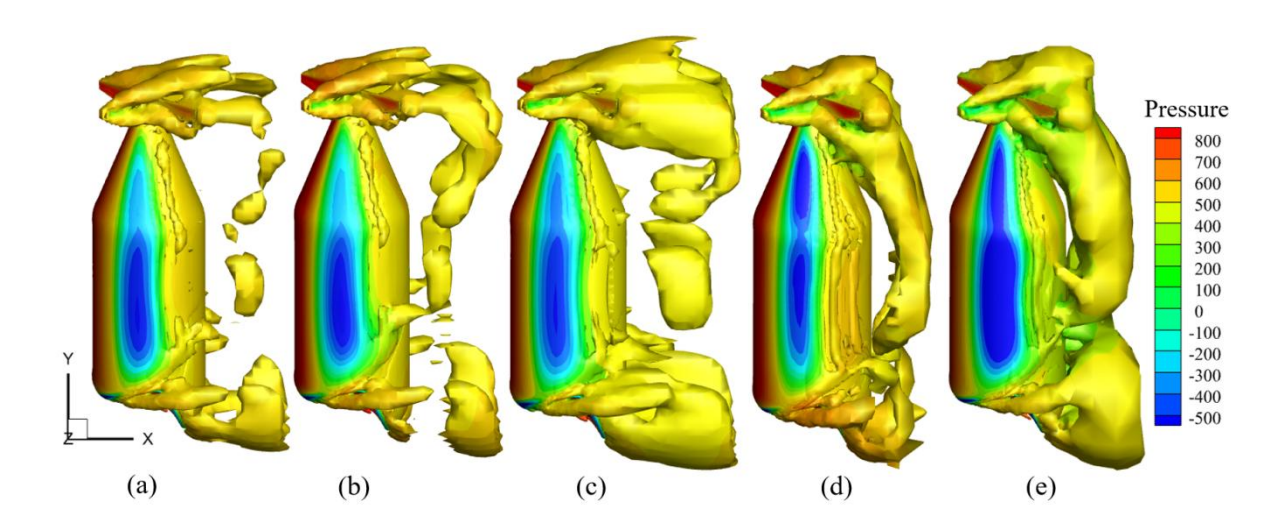


Fig. 5 The vortex and pressure distributions in the flow field around the submersible at different Reynolds numbers. (a) Re=21,916 (b) Re=43,948 (c) Re=65,749 (d) Re=87,666 (e) Re=109,582.

Parameters	Numerical value
Density	$1.3-1.4 g/cm^3$
Expansion rate	3%-5%
Water absorption rate	8%-11%
Tensile strength	300-740 <i>MPa</i>
Young's modulus	10-17 <i>GPa</i>
Elongation at break	15%-25%

Table 4 Experimenting with the physical properties of silk.

Table 5 Experimental design matrix for silk appendage configurations.

Group A (l/L)	Group B length combinations (l/L)
0	0, 0.05, 0.10, 0.15, 0.20, 0.25, 0.30, 0.35, 0.40
0.05	0, 0.05, 0.10, 0.15, 0.20, 0.25, 0.30, 0.35, 0.40
0.10	0, 0.05, 0.10, 0.15, 0.20, 0.25, 0.30, 0.35, 0.40
0.15	0, 0.05, 0.10, 0.15, 0.20, 0.25, 0.30, 0.35, 0.40

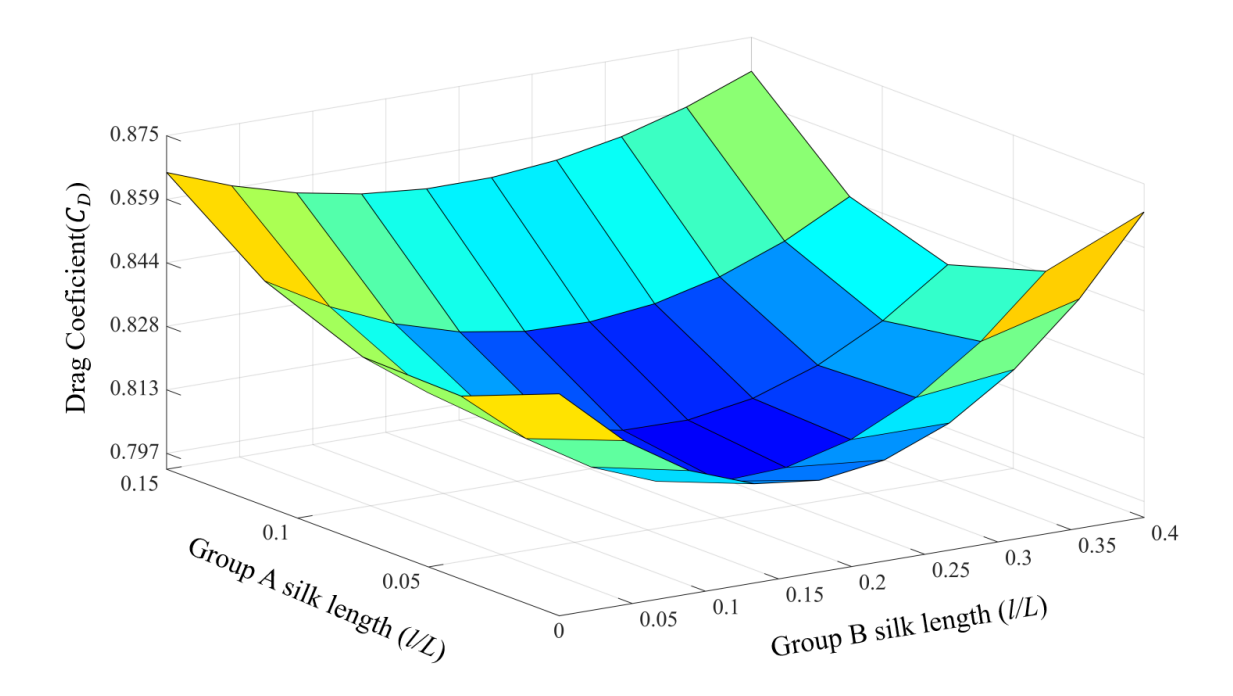


Fig. 6. Drag coefficient (C_D) versus normalized silk appendage length variation (l/L).

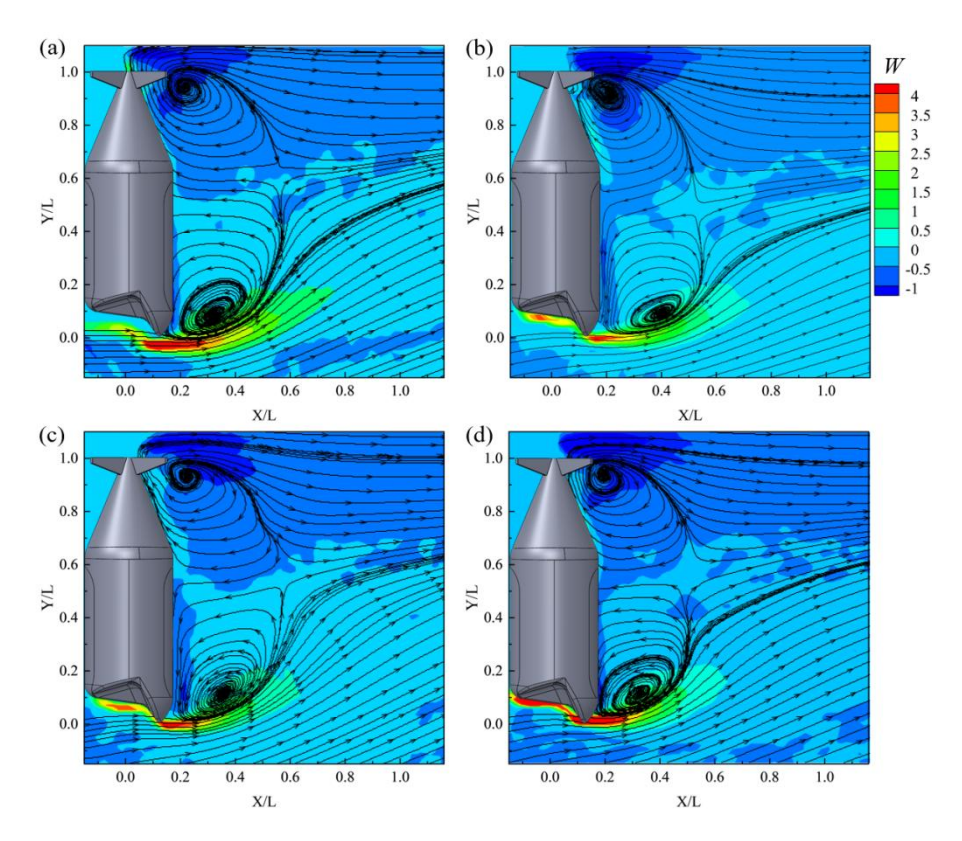


Fig. 7 Normalized time-averaged streamlines and vortex clouds of the submersible under different conditions. Case(a):(A=0 L, B=0 L), Case(b):(A=0 L, B=0.2 L), Case(c):(A=0.05 L, B=0.2 L), Case(d):(A=0.15 L, B=0.2 L).

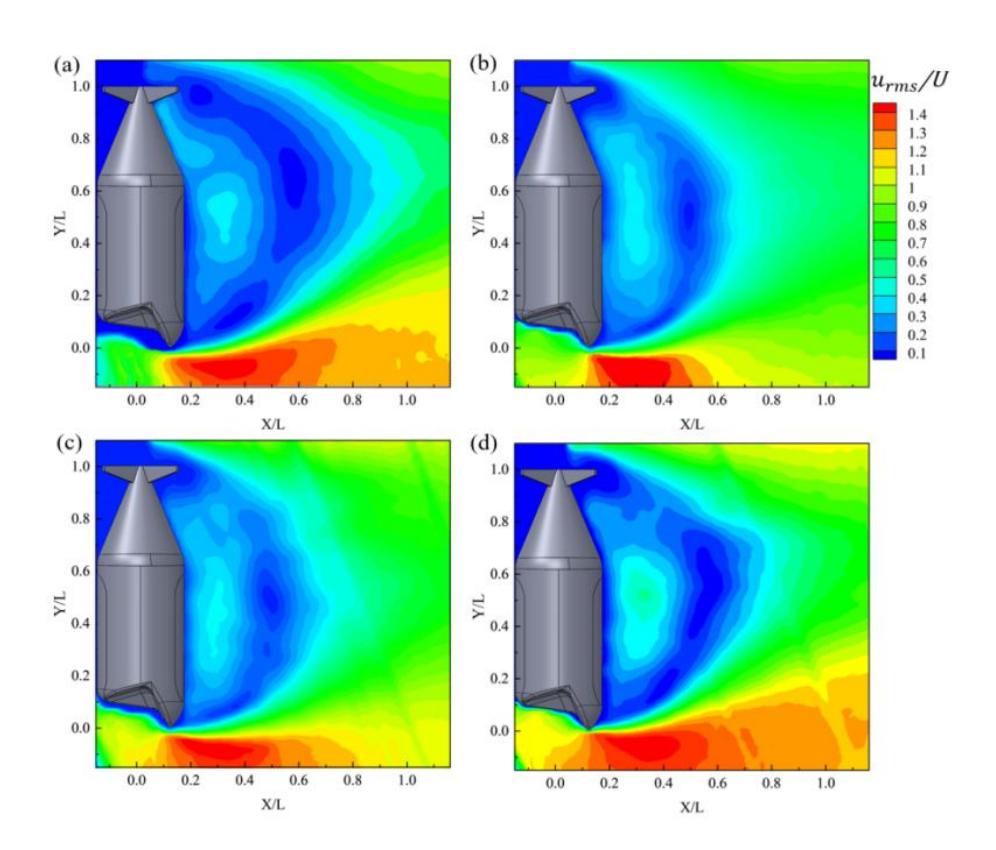


Fig. 8 Normalized Root Mean Square (RMS) velocity distributions of the submersible under different conditions. Case(a):(A=0 L, B=0 L), Case(b):(A=0 L, B=0.2 L), Case(c):(A=0.05 L, B=0.2 L), Case(d):(A=0.15 L, B=0.2 L).

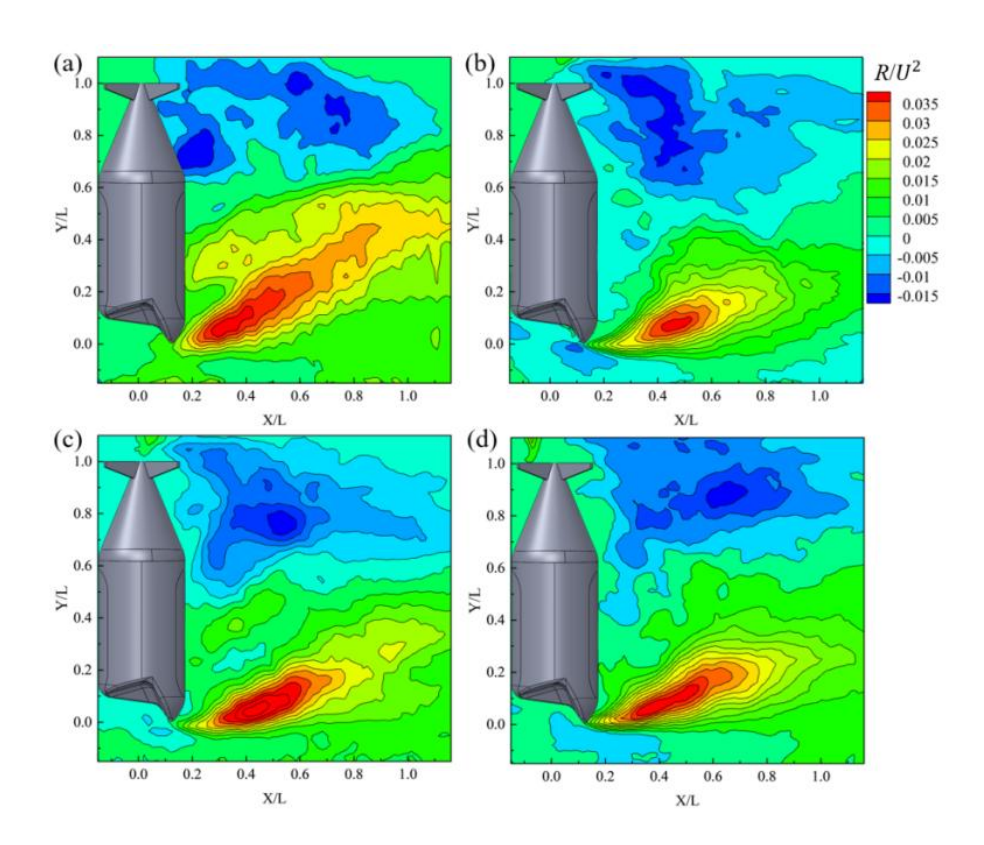


Fig. 9. Normalized Reynolds stress distribution of the submersible under different conditions.

Case(a):(A=0 L, B=0 L), Case(b):(A=0 L, B=0.2 L), Case(c):(A=0.05 L, B=0.2 L), Case(d):(A=0.15 L, B=0.2 L).

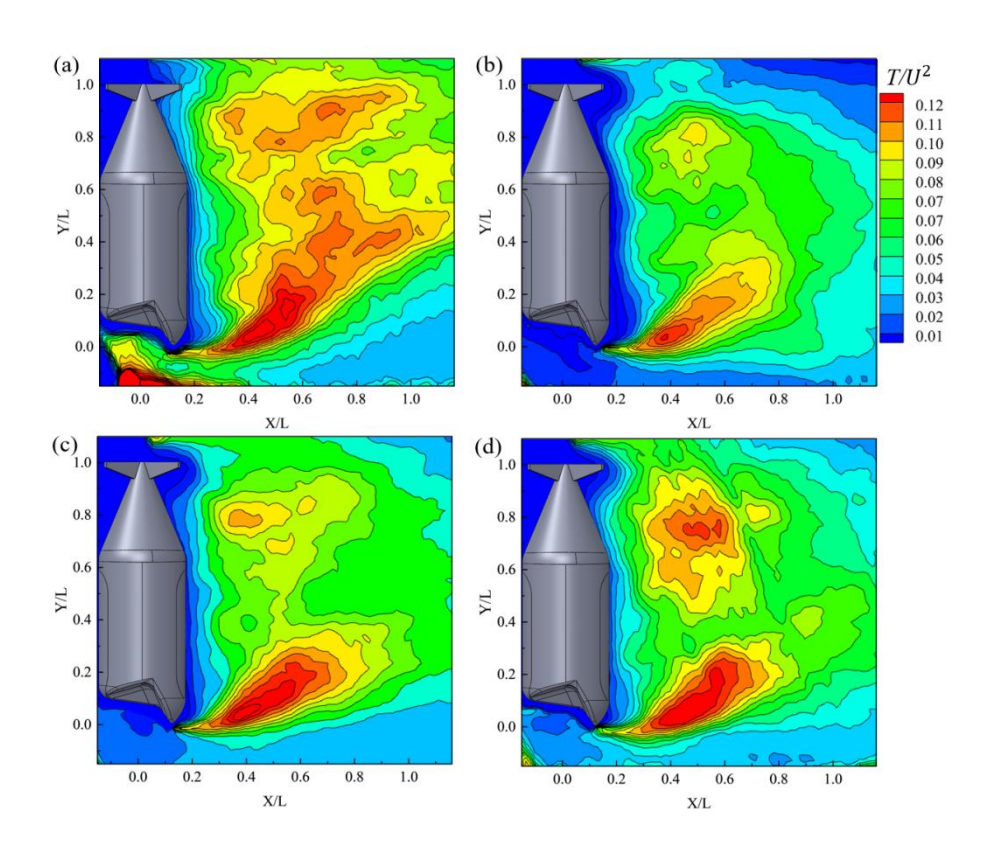


Fig. 10 Normalized turbulent kinetic energy cloud of the submersible under different conditions. Case(a):(A=0 L, B=0 L), Case(b):(A=0 L, B=0.2 L), Case(c):(A=0.05 L, B=0.2 L), Case(d):(A=0.15 L, B=0.2 L).

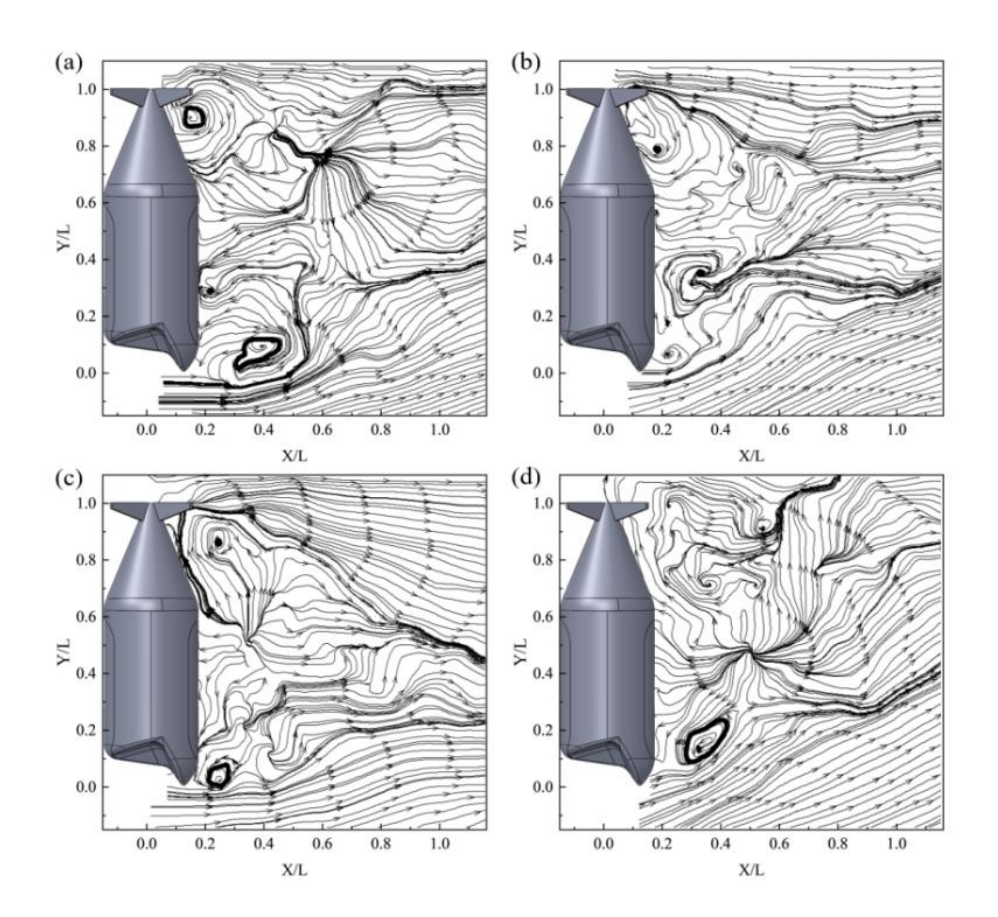


Fig. 11 Normalized instantaneous streamline distributions of the submersible at t = 7 s under different conditions. Case(a):(A=0 L, B=0 L), Case(b):(A=0 L, B=0.2 L), Case(c):(A=0.05 L, B=0.2 L), Case(d):(A=0.15 L, B=0.2 L).

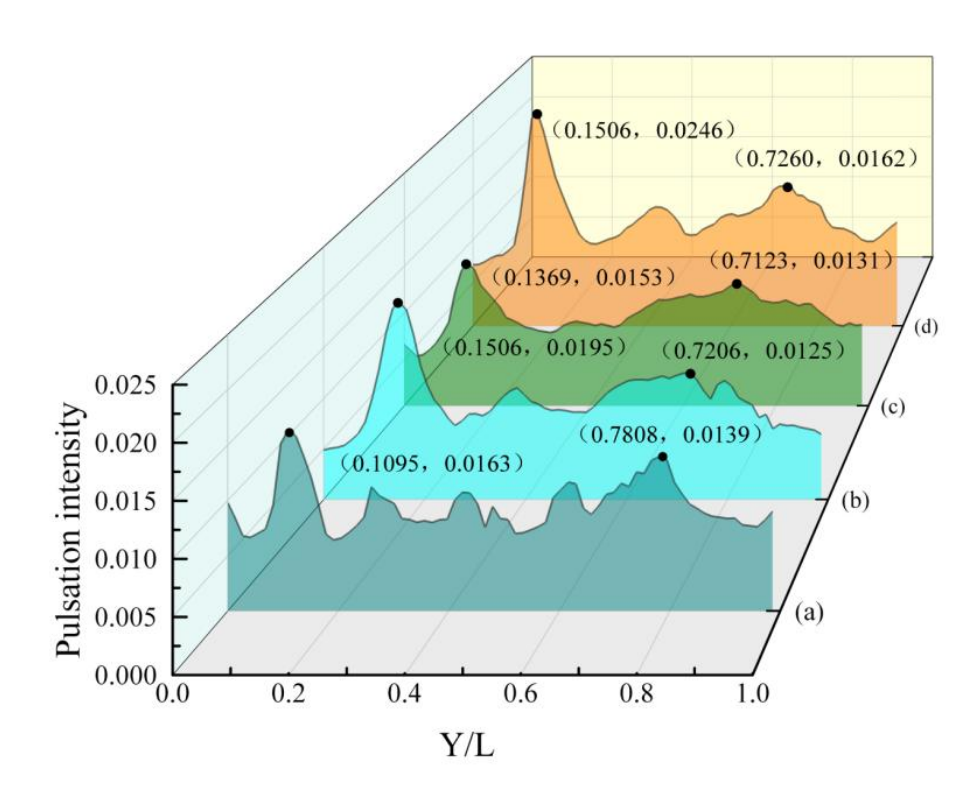


Fig. 12 Pulsation intensity fluctuation of the fluid along the normal y (Y/L) in the submersible flow field at X/L = 0.3. Case(a):(A=0 L, B=0 L), Case(b):(A=0 L, B=0.2 L), Case(c):(A=0.05 L, B=0.2 L), Case(d):(A=0.15 L, B=0.2 L).

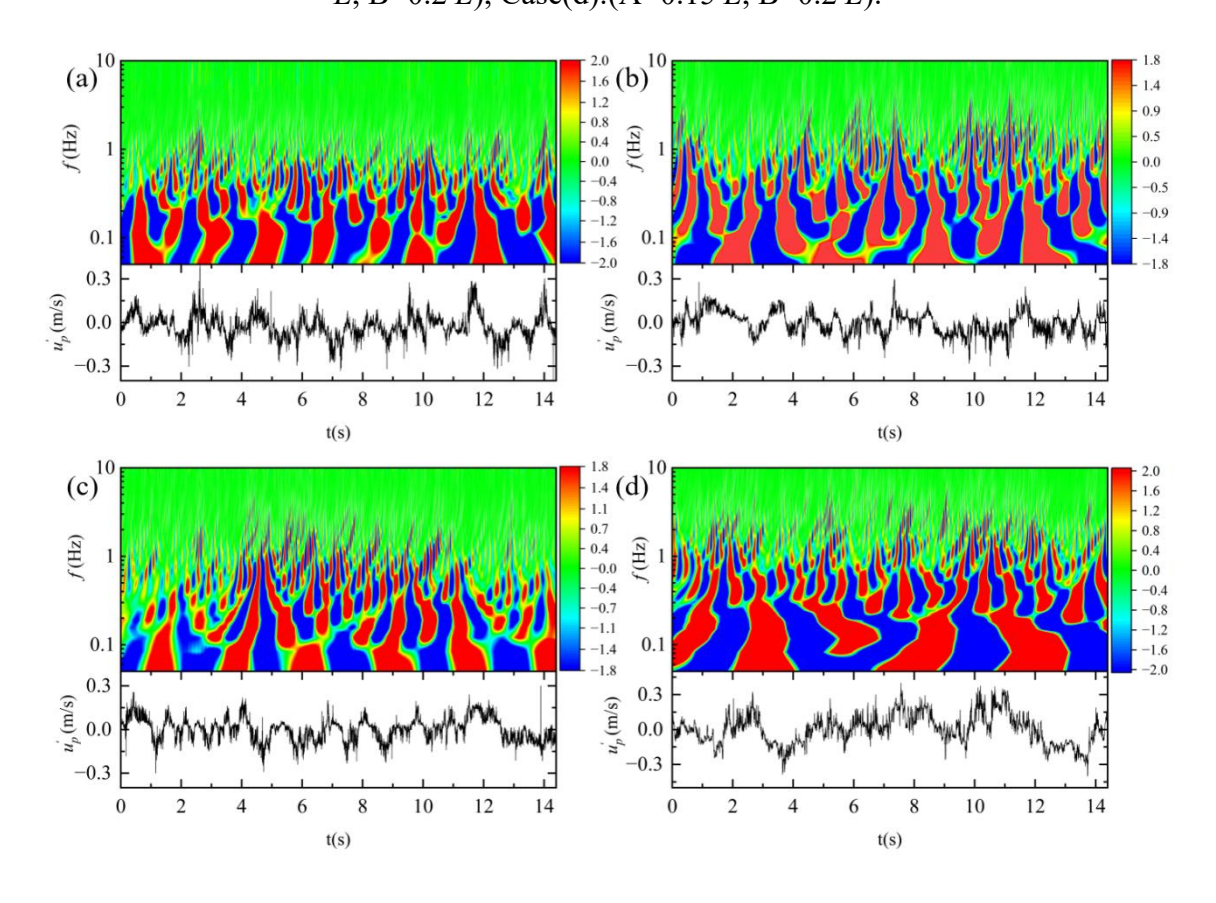


Fig. 13 Time-frequency distribution of x direction at (X/L = 0.3, Y/L = 0.1) for the submersible under different conditions. Case(a):(A=0 L, B=0 L), Case(b):(A=0 L, B=0.2 L), Case(c):(A=0.05 L, B=0.2 L), Case(d):(A=0.15 L, B=0.2 L).

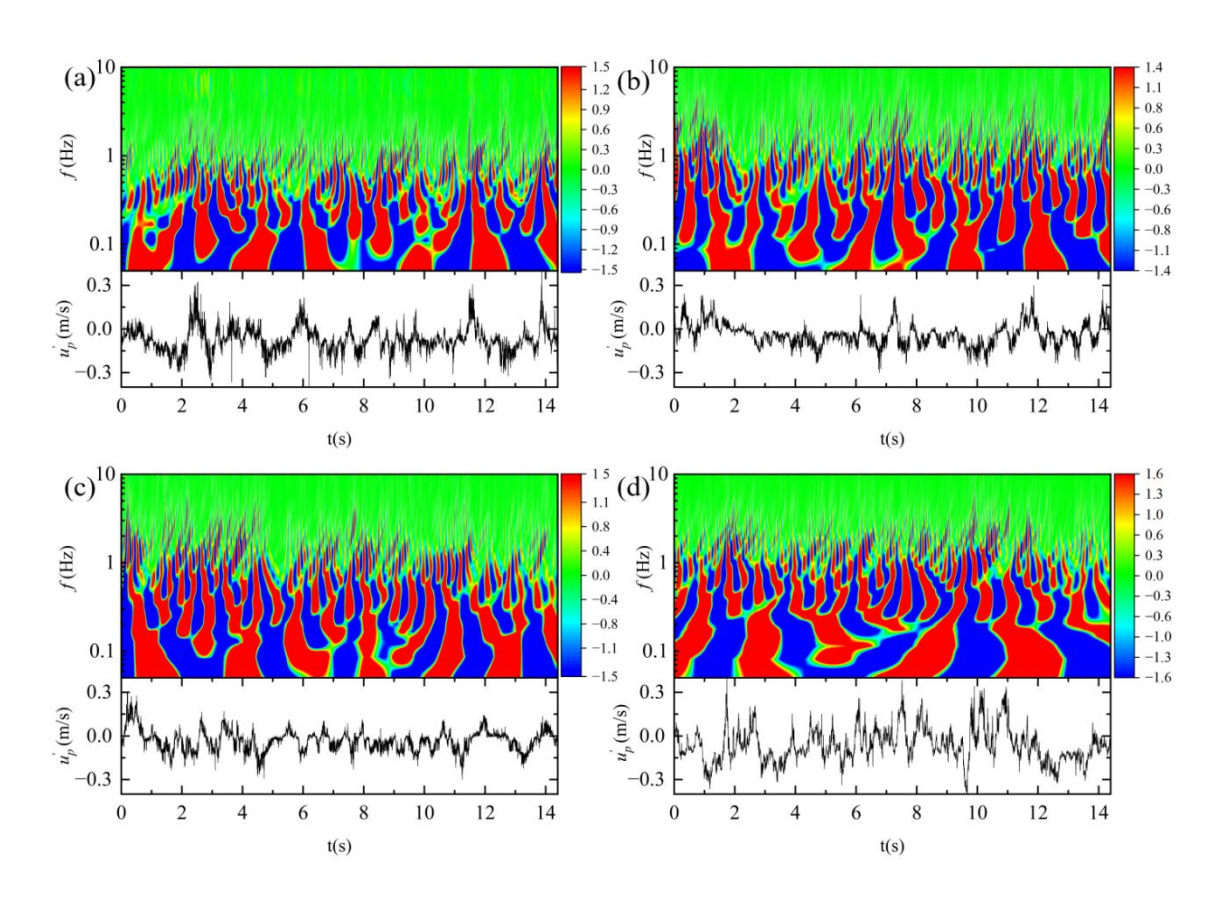


Fig. 14 Time-frequency distribution of y direction at (X/L = 0.3, Y/L = 0.1) for the submersible under different conditions. Case(a):(A=0 L, B=0 L), Case(b):(A=0 L, B=0.2 L), Case(c):(A=0.05 L, B=0.2 L), Case(d):(A=0.15 L, B=0.2 L).

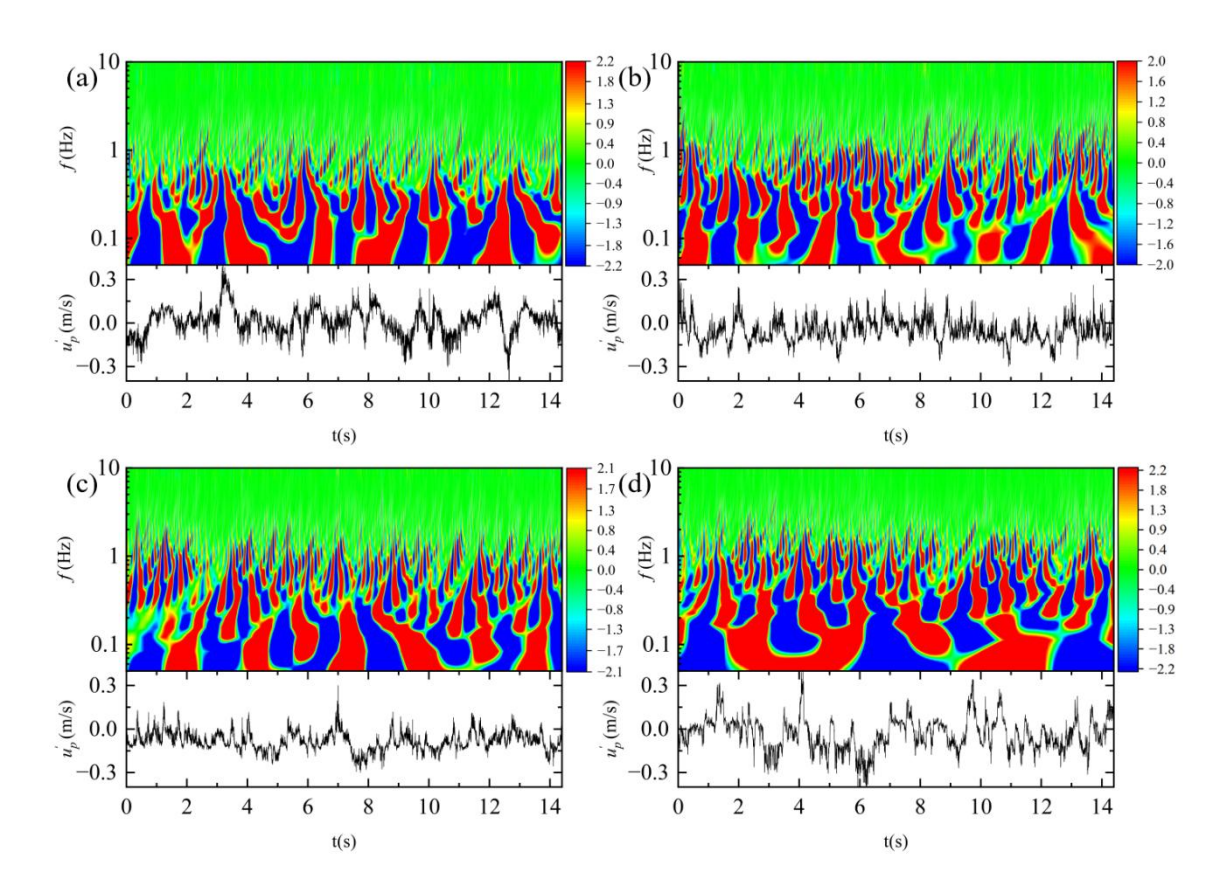


Fig. 15 Time-frequency distribution of x direction at (X/L = 0.3, Y/L = 0.9) for the submersible under different conditions. Case(a):(A=0 L, B=0 L), Case(b):(A=0 L, B=0.2 L), Case(c):(A=0.05 L, B=0.2 L), Case(d):(A=0.15 L, B=0.2 L).

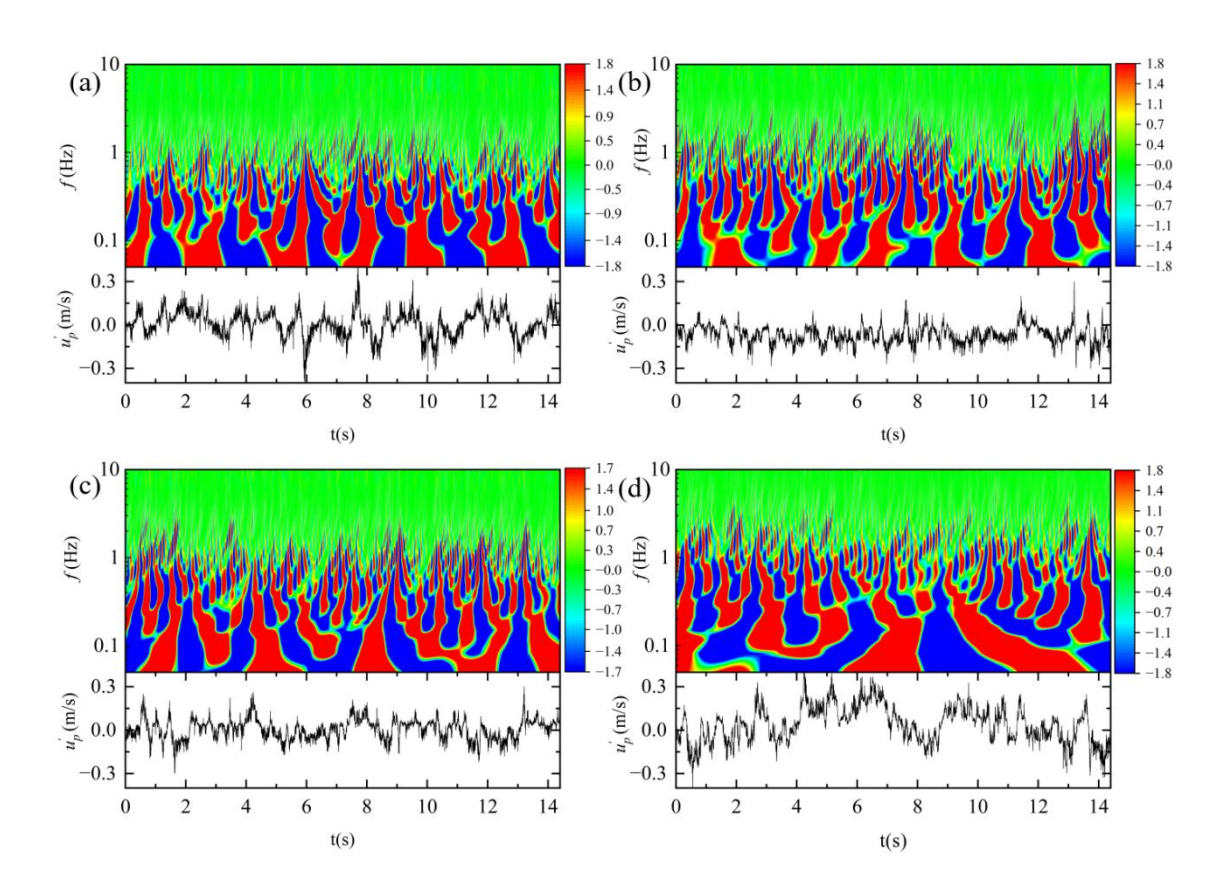


Fig. 16 Time-frequency distribution of y direction at (X/L = 0.3, Y/L = 0.9) for the submersible under different conditions. Case(a):(A=0 L, B=0 L), Case(b):(A=0 L, B=0.2 L), Case(c):(A=0.05 L, B=0.2 L), Case(d):(A=0.15 L, B=0.2 L).

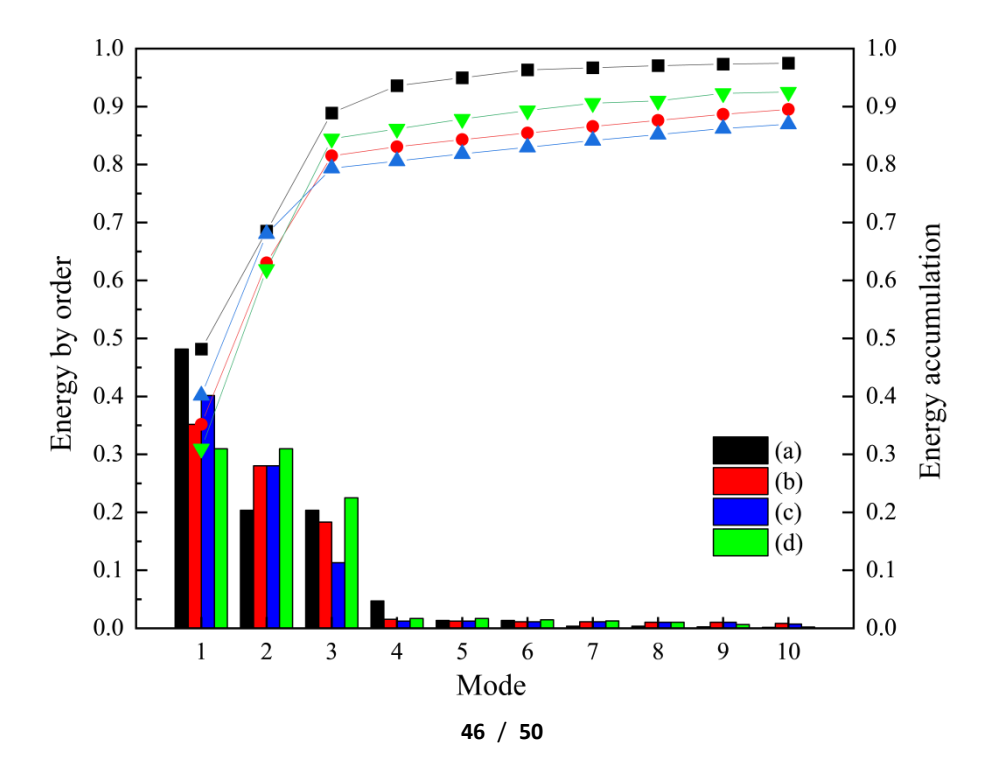


Fig. 17 Energy distribution and accumulation curves for the first 10 modal orders of the DMD for the submersible under different conditions.

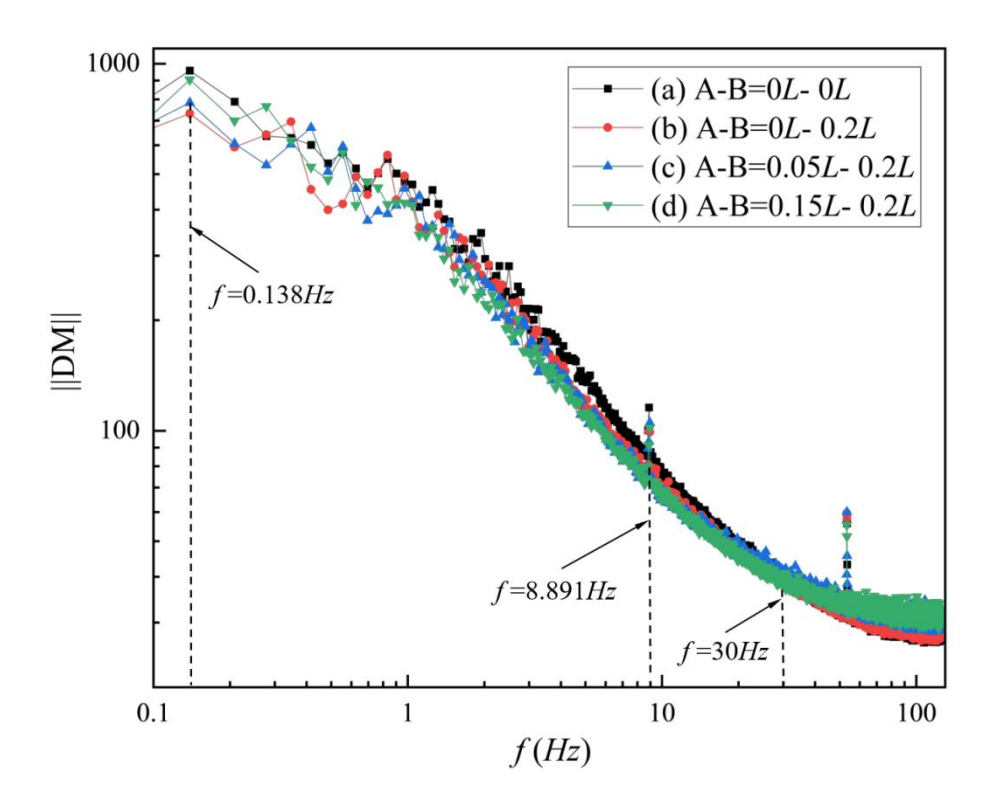


Fig. 18 DMD modal energy distribution of the submersible under various operating conditions.

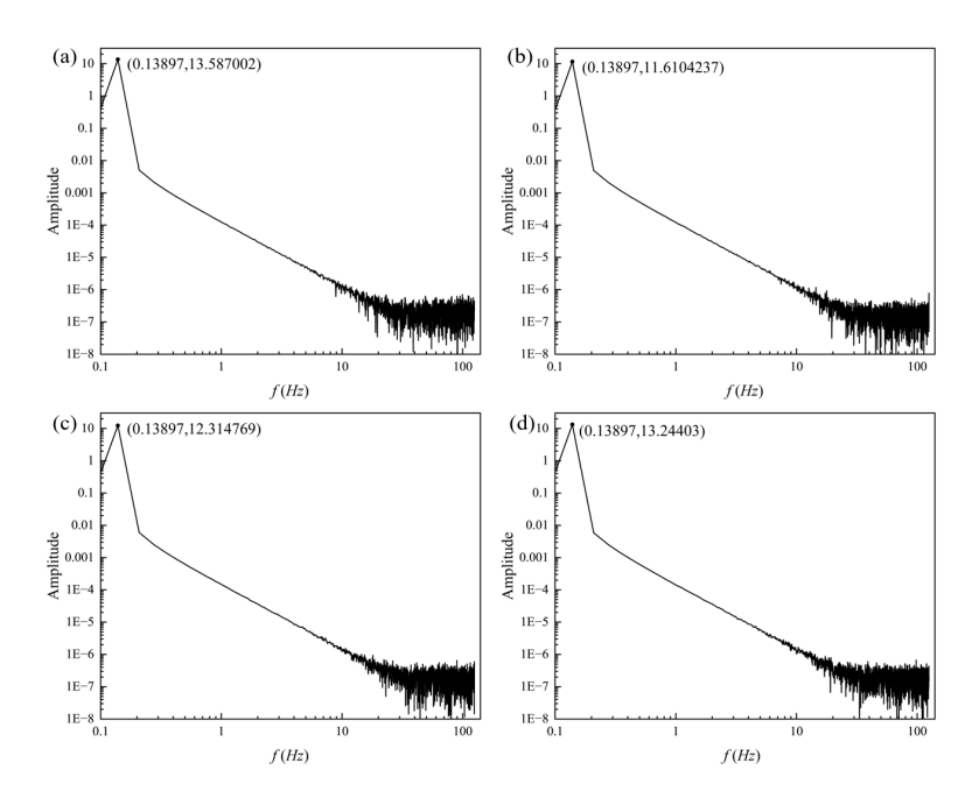
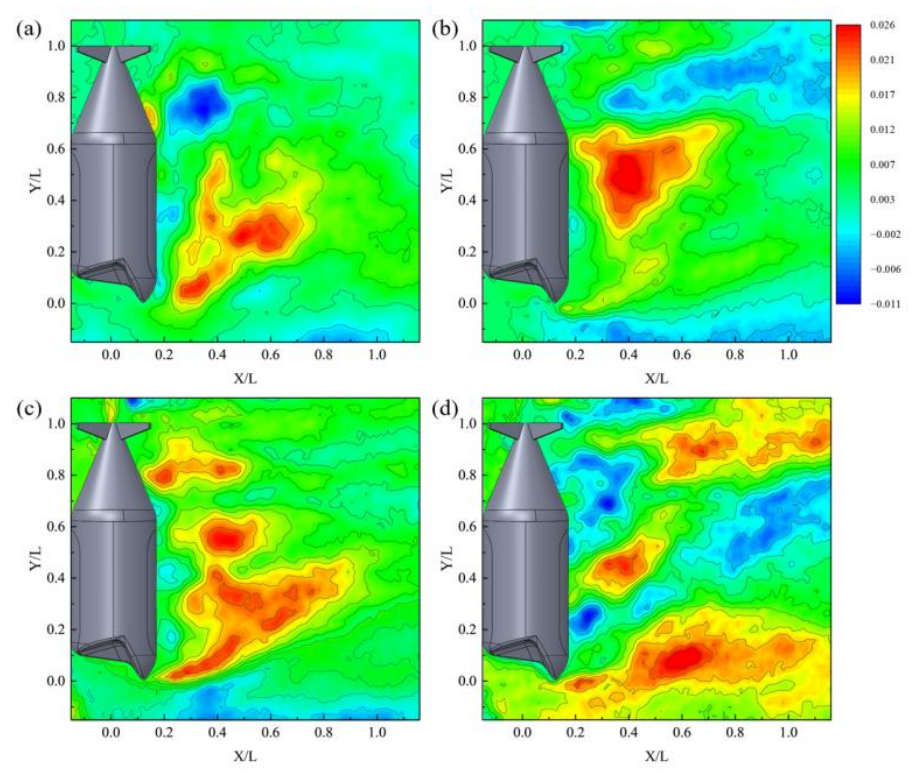


Fig. 19 Time coefficient spectra for each mode of the submersible under different conditions.

Case(a):(A=0 L, B=0 L), Case(b):(A=0 L, B=0.2 L), Case(c):(A=0.05 L, B=0.2 L), Case(d):(A=0.15 L, B=0.2 L).



48 / 50

Fig. 20 Normalized velocity field reconstruction of the submersible for the dominant mode (*f* = 0.13897 *Hz*) obtained through Dynamic Modal Decomposition (DMD) under different conditions. Case(a):(A=0 *L*, B=0 *L*), Case(b):(A=0 *L*, B=0.2 *L*), Case(c):(A=0.05 *L*, B=0.2 *L*), Case(d):(A=0.15 *L*, B=0.2 *L*).

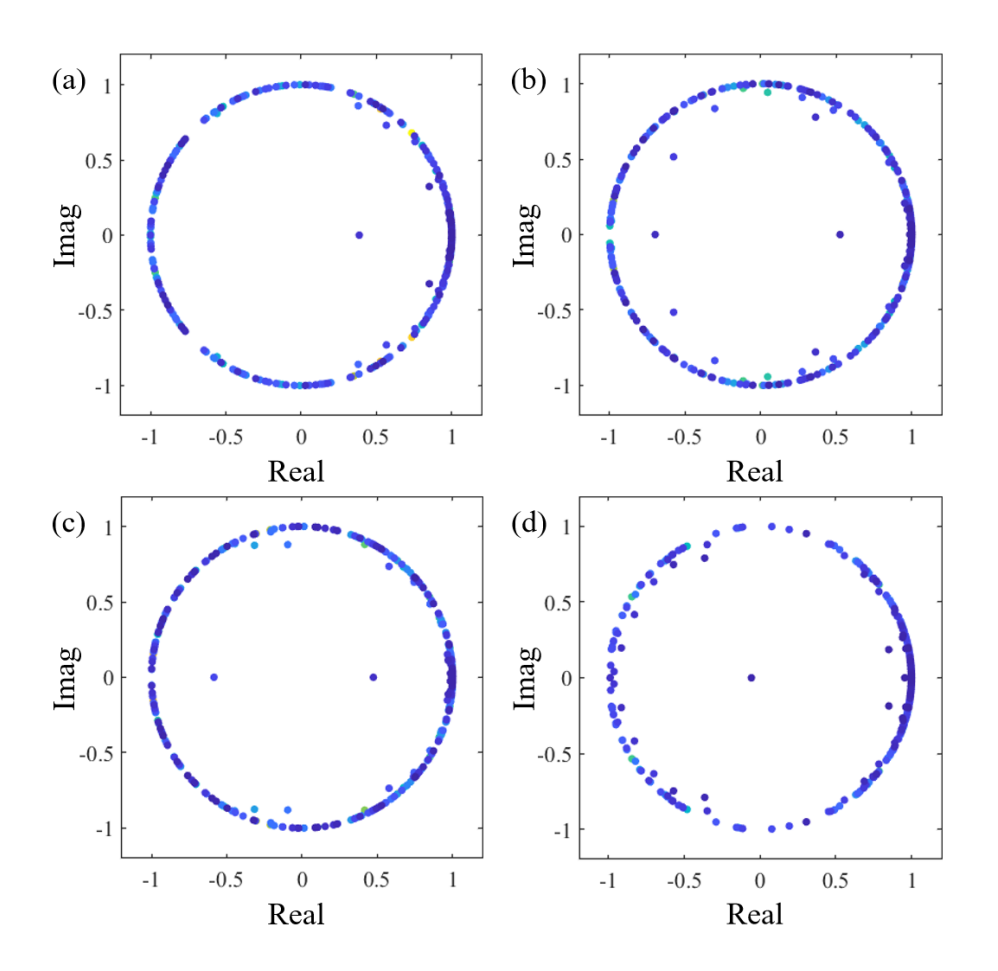


Fig. 21 Distribution of the real and imaginary parts of the DMD modal eigenroots on the unit circle for the submersible under different conditions. Case(a):(A=0 L, B=0 L), Case(b):(A=0 L, B=0.2 L), Case(c):(A=0.05 L, B=0.2 L), Case(d):(A=0.15 L, B=0.2 L).

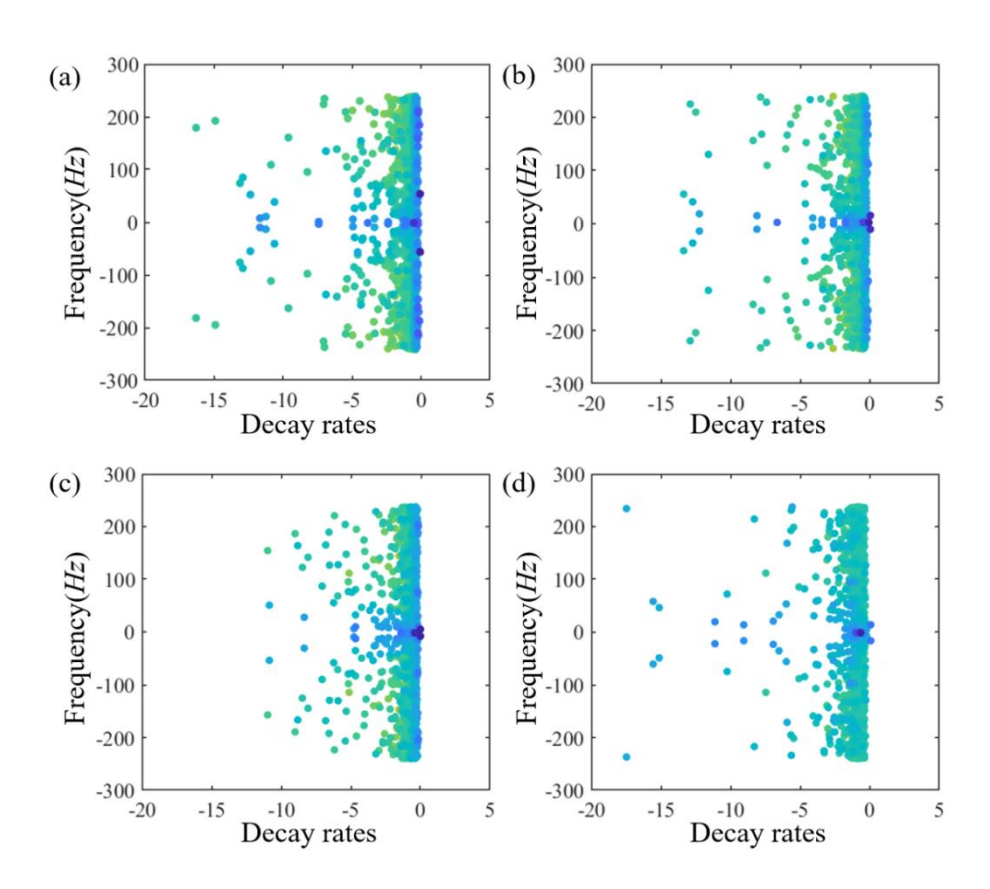


Fig. 22 Relationship between the DMD modal attenuation rate and frequency for the submersible under different conditions. Case(a):(A=0 L, B=0 L), Case(b):(A=0 L, B=0.2 L), Case(c):(A=0.05 L, B=0.2 L), Case(d):(A=0.15 L, B=0.2 L).